To cite this version :

A time semi-implicit scheme for the energy-balanced coupling of a shocked fluid flow with a deformable structure

Maria Adela Puscas [a,b,c,*], Laurent Monasse [a], Alexandre Ern [a],
Christian Tenaud [c], Christian Mariotti [b], Virginie Daru [c,d]

[a] *Université Paris-Est, CERMICS (ENPC), 77455 Marne la Vallée cedex, France*
[b] *CEA-DAM-DIF, 91297 Arpajon, France*
[c] *LIMSI-CNRS, Bât 508 Campus Universitaire, Rue John Von Neumann, 91403 Orsay Cedex, France*
[d] *Lab. DynFluid, Ensam, 75013 Paris, France*

A B S T R A C T

The objective of this work is to present a conservative coupling method between an inviscid compressible fluid and a deformable structure undergoing large displacements. The coupling method combines a cut-cell Finite Volume method, which is exactly conservative in the fluid, and a symplectic Discrete Element method for the deformable structure. A time semi-implicit approach is used for the computation of momentum and energy transfer between fluid and solid, the transfer being exactly balanced. The coupling method is exactly mass-conservative (up to round-off errors in the geometry of cut-cells) and exhibits numerically a long-time energy-preservation for the coupled system. The coupling method also exhibits consistency properties, such as conservation of uniform movement of both fluid and solid, absence of numerical roughness on a straight boundary, and preservation of a constant fluid state around a wall having tangential deformation velocity. The performance of the method is assessed on test cases involving shocked fluid flows interacting with two and three-dimensional deformable solids undergoing large displacements.

1. Introduction

Fluid–structure interaction phenomena occur in many fields, such as aeronautics, civil engineering, energetics, biology, and in the military and safety domains. In this context for instance, the effects of an explosion on a building involve complex non-linear phenomena (shock waves, cracking, fragmentation, etc.) [1,2], and the characteristic time scales of these phenomena are extremely short. The driving effect of the fluid–structure interaction is the fluid overpressure, and viscous effects play a lesser role. With an eye toward these applications, we consider an inviscid compressible flow with shock waves interacting with a deformable solid object.

Numerical methods for fluid–structure interaction can be broadly categorized into monolithic and partitioned methods. In monolithic (Eulerian [3,4] or Lagrangian [5,6]) methods, the fluid and the solid equations are solved simultaneously

at each time step. However, in many numerical schemes, the fluid is described in Eulerian formulation and the solid in Lagrangian formulation. This is possible in partitioned approaches where the fluid and the solid equations are solved separately, and an interface module is used to exchange information between the fluid and the solid solvers to enforce the dynamic boundary conditions at their common interface. Two main types of methods have been developed in this context: Arbitrary Lagrangian–Eulerian (ALE) methods [7,8] and fictitious domain methods [9–19]. The ALE method hinges on a mesh fitting the solid boundary, and therefore requires remeshing of the fluid domain when the solid goes through large displacements and topological changes due to fragmentation. Instead, fictitious domain methods, as those considered herein, work on a fixed fluid grid to which the solid is superimposed, and additional terms are introduced in the fluid formulation to impose the boundary conditions at the fluid–solid interface.

Conservative cut-cell Finite Volume methods for compressible fluid–structure interaction have been proposed by Noh [19]. Therein, a Lagrangian method for the solid is coupled with an Eulerian Finite Volume method for the compressible flow satisfying mass, momentum, and energy conservation in the fluid. Such methods have been used in a number of applications [10,11,14,15,19,20]. A coupling method between an inviscid compressible fluid and a rigid body undergoing large displacements has been developed in [21,22] using a cut-cell Finite Volume method. The coupling method is conservative in the sense that (i) mass, momentum, and energy conservation in the fluid is achieved by the cut-cell Finite Volume method as in [19], and (ii) the momentum and energy exchange between the fluid and the solid is balanced. As a result, the system is exactly conservative, up to round-off errors in the geometry of cut-cells. Moreover, the coupling method exhibits interesting consistency properties, such as conservation of uniform movement of both fluid and solid, and absence of numerical roughness on a straight boundary.

The main purpose of this work is to develop a three-dimensional conservative coupling method between a compressible inviscid fluid and a deformable solid undergoing large displacements. By conservative, we mean that properties (i) and (ii) above are satisfied, as in [21,22], and additionally that a symplectic scheme is used for the Lagrangian solid ensuring the conservation of a discrete energy (which is a close approximation of the physical energy). As a result, the coupled discrete system is not exactly energy-conservative, but we show numerically that our strategy yields long-time energy-preservation for the coupled system. Furthermore, as in [21,22], the Finite Volume method for the fluid is high-order in smooth flow regions and away from the solid boundary, while it is first-order near the shocks (due to the flux limiters) and in the vicinity of the solid boundary. Consequently, the coupling method is overall first-order accurate. Still, the use of a high-order method in smooth regions is useful to limit numerical diffusion in the fluid, as discussed in [23]. In any case, the coupling method, which is the focus of this work, is independent of the choice of the fluid fluxes.

While the core of the present method hinges on the techniques of [22] for a rigid solid, many new aspects have to be addressed. A reconstruction of the solid boundary around the solid assembly is needed since the solid deforms through the interaction with the fluid. Furthermore, a time semi-implicit scheme is introduced for the momentum and energy exchange, so as to take into account the deformation of the solid boundary during the time step. The advantage of this scheme with respect to an explicit one is to achieve additional consistency properties, such as the absence of pressure oscillations near a solid wall having only tangential deformation. The time semi-implicit scheme evaluates the fluid fluxes as well as the solid forces and torques only once per time step, which is important for computational efficiency of the scheme. Additionally, we prove that the time semi-implicit scheme converges with geometric rate under a CFL condition, which, under the assumption that the solid density is larger than the fluid density, is less restrictive than the fluid CFL condition.

The paper is organized as follows: Section 2 briefly describes the basic ingredients (which are common with [22]): the fluid and solid discretization methods and the cut-cell Finite Volume method. Section 3 presents the conservative coupling method based on the time semi-implicit procedure. Section 4 discusses several properties of the coupling method. Section 5 presents numerical results on strong fluid discontinuities interacting with two and three-dimensional deformable solids undergoing large displacements. Section 6 contains concluding remarks. Finally, Appendix A provides some background on the Discrete Element method used to discretize the solid, and Appendix B contains the convergence proof for the time semi-implicit scheme.

2. Basic ingredients

2.1. Fluid discretization

For inviscid compressible flow, the fluid state is governed by the Euler equations, which can be written in conservative form as

$$\frac{\partial}{\partial t}U + \frac{\partial}{\partial x}F(U) + \frac{\partial}{\partial y}G(U) + \frac{\partial}{\partial z}H(U) = 0, \tag{1}$$

where $U = (\rho, \rho u, \rho v, \rho w, \rho E)^t$ is the conservative variable vector and $F(U)$, $G(U)$, and $H(U)$ indicate the inviscid fluxes

$$F(U) = \begin{pmatrix} \rho u \\ \rho u^2 + p \\ \rho u v \\ \rho u w \\ (\rho E + p)u \end{pmatrix}, \quad G(U) = \begin{pmatrix} \rho v \\ \rho u v \\ \rho v^2 + p \\ \rho v w \\ (\rho E + p)v \end{pmatrix}, \quad H(U) = \begin{pmatrix} \rho w \\ \rho u w \\ \rho v w \\ \rho w^2 + p \\ (\rho E + p)w \end{pmatrix},$$

with ρ the mass density, p the pressure, (u, v, w) the Cartesian components of the velocity vector $\vec{u}$, and E the total energy. The system is closed by the equation of state for ideal gas: $p = (\gamma - 1)\rho e$, e being the specific internal energy with $E = e + \frac{1}{2}(u^2 + v^2 + w^2)$ and γ the ratio of specific heats ($\gamma = 1.4$ for air).

The discretization of these equations is based on an explicit Finite Volume method on a Cartesian grid. We denote with integer subscripts i, j, k quantities related to the center of cells and with half-integer subscripts quantities related to the center of faces of cells. For instance, the interface between cells $C_{i,j,k}$ and $C_{i+1,j,k}$ is denoted by $\partial C_{i+\frac{1}{2},j,k}$. The time step, which is subjected to a CFL condition, is taken constant for simplicity and is denoted Δt. We introduce the discrete times $t^n = n\Delta t$, for all $n \geq 0$. Let $C_{i,j,k}$ be a fluid cell of size $(\Delta x_{i,j,k}, \Delta y_{i,j,k}, \Delta z_{i,j,k})$. The Finite Volume scheme for the fluid in the absence of the solid takes the form

$$U_{i,j,k}^{n+1} = U_{i,j,k}^n + \Delta t\, \Phi_{i,j,k}^{n+1/2}, \tag{2}$$

with the flux $\Phi_{i,j,k}^{n+1/2}$ given by

$$\Phi_{i,j,k}^{n+1/2} = \frac{F_{i-1/2,j,k}^{n+1/2} - F_{i+1/2,j,k}^{n+1/2}}{\Delta x_{i,j,k}} + \frac{G_{i,j-1/2,k}^{n+1/2} - G_{i,j+1/2,k}^{n+1/2}}{\Delta y_{i,j,k}} + \frac{H_{i,j,k-1/2}^{n+1/2} - H_{i,j,k+1/2}^{n+1/2}}{\Delta z_{i,j,k}}, \tag{3}$$

where $U_{i,j,k}^n$ is a numerical approximation of the exact solution over the cell $C_{i,j,k}$ at time t^n, and $F_{i\pm1/2,j,k}^{n+1/2}$, $G_{i,j\pm1/2,k}^{n+1/2}$, $H_{i,j,k\pm1/2}^{n+1/2}$ are numerical fluxes approximating the time-average of the corresponding physical flux over the time interval $[t^n, t^{n+1}]$ and evaluated at $\partial C_{i\pm\frac{1}{2},j,k}$, $\partial C_{i,j\pm\frac{1}{2},k}$, and $\partial C_{i,j,k\pm\frac{1}{2}}$, respectively. In the present work, we use the one-dimensional OSMP scheme [23] of formal order 11 in smooth regions. The three-dimensional extension is achieved through a directional operator splitting which is second-order accurate.

2.2. Solid discretization

The deformable moving solid is discretized by the Discrete Element method using a finite number of rigid particles. Each particle is governed by the classical equations of mechanics. The particles interact through forces and torques. The expression of these forces and torques allows one to recover the macroscopic behavior of the solid [24,25]. We observe that an attractive feature of the Discrete Element method is that it facilitates the handling of rupture by breaking the link between solid particles.

The particles have a polyhedral shape and are assumed to be star-shaped with respect to their center of mass, and their faces are assumed to be star-shaped with respect to their center of mass. We assume that the diameter of the largest inscribed sphere in the solid is larger than two fluid grid cells.

A generic solid particle I is characterized by the following quantities: the mass m_I, the diameter $h_{s,I}$, the position of the center of mass X_I, the velocity of the center of mass $\vec{V}_I$, the rotation matrix $\mathbf{Q}_I$, the angular momentum matrix $\mathbf{P}_I$, and the principal moments of inertia I_I^i, $i \in \{1, 2, 3\}$. Let $\mathbf{D}_I = \mathrm{diag}(d_I^1, d_I^2, d_I^3)$ with $d_I^i = \frac{1}{2}\left(I_I^1 + I_I^2 + I_I^3\right) - I_I^i$, $i \in \{1, 2, 3\}$.

The explicit time-integration scheme for the solid in the absence of the fluid consists of the Verlet scheme for translation and the RATTLE scheme for rotation. For particle I, it takes the form

$$\vec{V}_I^{n+\frac{1}{2}} = \vec{V}_I^n + \frac{\Delta t}{2m_I}\vec{F}_{I,\mathrm{int}}^n, \tag{4}$$

$$X_I^{n+1} = X_I^n + \Delta t\, \vec{V}_I^{n+\frac{1}{2}}, \tag{5}$$

$$\mathbf{P}_I^{n+\frac{1}{2}} = \mathbf{P}_I^n + \frac{\Delta t}{4}\mathbf{j}(\vec{\mathcal{M}}_{I,\mathrm{int}}^n)\mathbf{Q}_I^n + \frac{\Delta t}{2}\mathbf{\Upsilon}_I^n\mathbf{Q}_I^n, \tag{6}$$

$$\mathbf{Q}_I^{n+1} = \mathbf{Q}_I^n + \Delta t\,\mathbf{P}_I^{n+\frac{1}{2}}\mathbf{D}_I^{-1}, \tag{7}$$

$$\vec{V}_I^{n+1} = \vec{V}_I^{n+\frac{1}{2}} + \frac{\Delta t}{2m_I}\vec{F}_{I,\mathrm{int}}^{n+1}, \tag{8}$$

$$\mathbf{P}_I^{n+1} = \mathbf{P}_I^{n+\frac{1}{2}} + \frac{\Delta t}{4}\mathbf{j}(\vec{\mathcal{M}}_{I,\mathrm{int}}^{n+1})\mathbf{Q}_I^{n+1} + \frac{\Delta t}{2}\tilde{\mathbf{\Upsilon}}_I^{n+1}\mathbf{Q}_I^{n+1}, \tag{9}$$

where in (6), $\mathbf{\Upsilon}_I^n$ is a symmetric matrix such that

$$(\mathbf{Q}_I^{n+1})^t\mathbf{Q}_I^{n+1} = \mathbf{I}, \tag{10}$$

with $\mathbf{I}$ the identity matrix in $\mathbb{R}^3$, and in (9), $\tilde{\mathbf{\Upsilon}}_I^{n+1}$ is a symmetric matrix such that

$$(\mathbf{Q}_I^{n+1})^t\mathbf{P}_I^{n+1}\mathbf{D}_I^{-1} + \mathbf{D}_I^{-1}(\mathbf{P}_I^{n+1})^t\mathbf{Q}_I^{n+1} = \mathbf{0}. \tag{11}$$
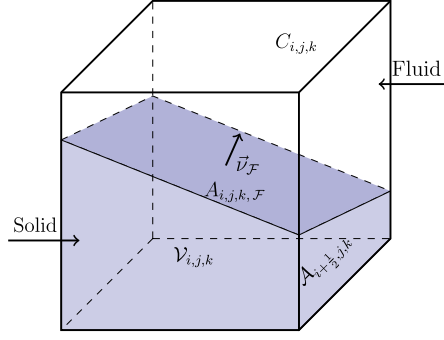
Fig. 1. Illustration of a cut-cell $C_{i,j,k}$.

The matrices $\mathbf{\Upsilon}_I^n$ and $\tilde{\mathbf{\Upsilon}}_I^{n+1}$ are the Lagrange multipliers associated with the constraints (10) and (11), see [21]. The map $\mathbf{j} : \mathbb{R}^3 \to \mathbb{R}^{3 \times 3}$ is such that $\mathbf{j}(\vec{x})\vec{y} = \vec{x} \wedge \vec{y}$ for all $\vec{x}, \vec{y} \in \mathbb{R}^3$. The force $\vec{F}_{I,\text{int}}^n$ and torque $\vec{\mathcal{M}}_{I,\text{int}}^n$ result from the interaction of particle I with its neighbouring particles, see Appendix A for the expression of these quantities.

The time-integration scheme for the solid being explicit, the time step is restricted by a CFL condition. This condition states that the displacement of each solid particle I during one time-step should be less than the characteristic size of the particle $h_{s,I}$ and the rotation of each particle I during one time-step should be less than $\frac{\pi}{8}$ (see [21]).

In the case of fluid–structure interaction with immersed boundaries, in addition to the fluid and solid CFL conditions, the time step is also restricted so that the displacement of the solid is less than one fluid grid cell size in the course of the time step, so that the solid boundary crosses at most one fluid grid cell per time-step. This condition is less stringent than the fluid CFL condition since the fluid in the vicinity of the solid boundary should have a velocity at least equal to that of the solid.

2.3. Cut-cell finite volume discretization

The faces of the solid particles in contact with the fluid are collected in the set $\mathfrak{F}$. A generic element of $\mathfrak{F}$ is denoted by $\mathcal{F}$ and is called a wet solid face. The fluid–solid interface consists of all the wet solid faces. Owing to the movement of the solid, the wet solid faces are time-dependent sets in $\mathbb{R}^3$, and we set $\mathcal{F}^n = \mathcal{F}(t^n)$ for all $n \geq 0$. Each wet solid face $\mathcal{F}(t)$ is characterized by its surface $A_{\mathcal{F}}(t)$ and its normal $\vec{v}_{\mathcal{F}}(t)$ (pointing from the solid to the fluid). Finally, we denote by $\Omega_{\text{solid}}(t)$ the solid domain and by $\Omega_{\text{fluid}}(t)$ the fluid domain.

The time-integration scheme is based on a partitioned approach where the coupling is achieved through boundary conditions at the fluid–solid interface. In our case, for an inviscid fluid, we consider perfect slip boundary conditions:

$$\vec{u}_{\text{fluid}} \cdot \vec{v}_{\text{fluid}} + \vec{u}_{\text{solid}} \cdot \vec{v}_{\text{solid}} = 0, \quad \boldsymbol{\sigma}_{\text{fluid}} \cdot \vec{v}_{\text{fluid}} + \boldsymbol{\sigma}_{\text{solid}} \cdot \vec{v}_{\text{solid}} = 0,$$

where $\vec{u}_{\text{fluid}}$ and $\vec{u}_{\text{solid}}$, $\boldsymbol{\sigma}_{\text{fluid}}$ and $\boldsymbol{\sigma}_{\text{solid}}$, $\vec{v}_{\text{fluid}}$ and $\vec{v}_{\text{solid}}$ are respectively the velocities, stresses, and outward pointing normals for the fluid and the solid.

In the Immersed Boundary method, the solid is superimposed to the fluid grid, leading to fluid–solid mixed cells, thereafter called "cut-cells". Let $C_{i,j,k}$ be a cut-cell. The relevant geometric quantities describing the intersection between the moving solid and the cell $C_{i,j,k}$ are (see Fig. 1):

- The **volume fraction** $0 \leqslant \Lambda_{i,j,k}^n \leqslant 1$ occupied by the solid in the cell $C_{i,j,k}$ at time t^n.
- The **side area fraction** $0 \leqslant \lambda_{i \pm \frac{1}{2}, j, k}^{n+\frac{1}{2}}, \lambda_{i, j \pm \frac{1}{2}, k}^{n+\frac{1}{2}}, \lambda_{i, j, k \pm \frac{1}{2}}^{n+\frac{1}{2}} \leqslant 1$ of each fluid grid cell face averaged over the time interval $\left[t^n, t^{n+1}\right]$.
- The **boundary area** $A_{i,j,k,\mathcal{F}}^{n+\frac{1}{2}}$ defined as the area of the intersection of the wet solid face $\mathcal{F}(t)$ with $C_{i,j,k}$ averaged over the time interval $\left[t^n, t^{n+1}\right]$.

The three-dimensional geometric algorithms used for the detection of the cut-cells and the computation of the intersection between the solid and the fluid grid are described in [22].

On the fluid side, we take into account the presence of the solid by modifying the fluid fluxes in cut-cells. Consider a cut-cell as illustrated in Fig. 1. The computation of the time-average of the side area fractions $\lambda^{n+\frac{1}{2}}$ (for simplicity, subscripts related to the fluid grid cells or their faces are omitted when they play no relevant role) and of the boundary area $A_{\mathcal{F}}^{n+\frac{1}{2}}$, as considered in [10], can be very complex in three space dimensions. Instead, as in [21], we evaluate the side area fraction and the boundary area at time t^{n+1} and compute the amount swept by the movement of the wet solid face $\mathcal{F}$ during the time step from t^n to t^{n+1} in order to enforce the discrete conservation of the conservative variables. This leads to the following approximation of (1):

$$\left(1 - \Lambda_{i,j,k}^{n+1}\right) U_{i,j,k}^{n+1} = \left(1 - \Lambda_{i,j,k}^{n+1}\right) U_{i,j,k}^{n} + \Delta t \, \Phi_{i,j,k,\,\text{fluid}}^{n+1} + \Delta t \, \Phi_{i,j,k,\,\text{solid}}^{n+1} + \Delta U_{i,j,k}^{n,n+1}. \tag{12}$$

The fluid flux $\Phi_{\text{fluid}}^{n+1}$ is now given by (compare with (3))

$$\Phi_{i,j,k,\,\text{fluid}}^{n+1} = \frac{\left(1 - \lambda_{i-\frac{1}{2},j,k}^{n+1}\right) F_{i-\frac{1}{2},j,k}^{n+\frac{1}{2}} - \left(1 - \lambda_{i+\frac{1}{2},j,k}^{n+1}\right) F_{i+\frac{1}{2},j,k}^{n+\frac{1}{2}}}{\Delta x_{i,j,k}}$$
$$+ \frac{\left(1 - \lambda_{i,j-\frac{1}{2},k}^{n+1}\right) G_{i,j-\frac{1}{2},k}^{n+\frac{1}{2}} - \left(1 - \lambda_{i,j+\frac{1}{2},k}^{n+1}\right) G_{i,j+\frac{1}{2},k}^{n+\frac{1}{2}}}{\Delta y_{i,j,k}}$$
$$+ \frac{\left(1 - \lambda_{i,j,k-\frac{1}{2}}^{n+1}\right) H_{i,j,k-\frac{1}{2}}^{n+\frac{1}{2}} - \left(1 - \lambda_{i,j,k+\frac{1}{2}}^{n+1}\right) H_{i,j,k+\frac{1}{2}}^{n+\frac{1}{2}}}{\Delta z_{i,j,k}}. \tag{13}$$

The solid flux $\Phi_{\text{solid}}^{n+1}$ resulting from the presence of the solid boundaries in the cell is given by

$$\Phi_{i,j,k,\,\text{solid}}^{n+1} = \frac{1}{V_{i,j,k}} \sum_{\{\mathcal{F} \in \mathfrak{F} \,|\, \mathcal{F}^{n+1} \cap C_{i,j,k} \neq \emptyset\}} \phi_{i,j,k,\,\mathcal{F}}^{n+1},$$

where $V_{i,j,k}$ is the volume of $C_{i,j,k}$ and $\phi_{\mathcal{F}}^{n+1}$ is the solid flux attached to the wet solid face $\mathcal{F}$. The detailed procedure to compute the solid flux is described in Section 3.4. Finally, the swept amount is given by

$$\Delta U_{i,j,k}^{n,n+1} = \sum_{\{\mathcal{F} \in \mathfrak{F} \,|\, \mathcal{F}^{n+1} \cap C_{i,j,k} \neq \emptyset\}} \Delta U_{i,j,k,\,\mathcal{F}}^{n,n+1},$$

where the term $\Delta U_{\mathcal{F}}^{n,n+1}$ denotes the amount of U swept by the movement of the wet solid face $\mathcal{F}$ during the time step from t^n to t^{n+1}. The detailed procedure to compute these quantities is described in [22], see also [21]. In the cut-cells where the volume fraction Λ is grater than 0.5, we use the conservative mixing described in [15,21,22]. In order to compute the fluid fluxes near the fluid–solid interface, we define an artificial state in the cells fully occupied by the solid from the states in the mirror cells relatively to the fluid–solid interface, as described in [22]. The number of mirror cells is typically of the order of the stencil for the fluid fluxes.

3. Time semi-implicit coupling with a deformable structure

3.1. Solid in presence of fluid

On the solid side, Eqs. (4), (6), (8), and (9), are modified by taking into account the fluid forces and torques applied to the particle I as follows:

$$\vec{V}_I^{n+\frac{1}{2}} = \vec{V}_I^n + \frac{\Delta t}{2m_I}(\vec{F}_{I,\text{int}}^n + \vec{F}_{I,\text{fluid}}^{n+1}), \tag{14}$$

$$\mathbf{P}_I^{n+\frac{1}{2}} = \mathbf{P}_I^n + \frac{\Delta t}{4}\mathbf{j}(\vec{\mathcal{M}}_{I,\text{int}}^n + \vec{\mathcal{M}}_{I,\text{fluid}}^{n+1})\mathbf{Q}_I^n + \frac{\Delta t}{2}\Upsilon_I^n\mathbf{Q}_I^n, \tag{15}$$

$$\vec{V}_I^{n+1} = \vec{V}_I^{n+\frac{1}{2}} + \frac{\Delta t}{2m_I}(\vec{F}_{I,\text{int}}^{n+1} + \vec{F}_{I,\text{fluid}}^{n+1}), \tag{16}$$

$$\mathbf{P}_I^{n+1} = \mathbf{P}_I^{n+\frac{1}{2}} + \frac{\Delta t}{4}\mathbf{j}(\vec{\mathcal{M}}_{I,\text{int}}^{n+1} + \vec{\mathcal{M}}_{I,\text{fluid}}^{n+1})\mathbf{Q}_I^{n+1} + \frac{\Delta t}{2}\tilde{\Upsilon}_I^{n+1}\mathbf{Q}_I^{n+1}, \tag{17}$$

where $\vec{F}_{I,\text{fluid}}^{n+1}$ and $\vec{\mathcal{M}}_{I,\text{fluid}}^{n+1}$ are the fluid forces and torques applied to the particle I. An important point, as reflected by the superscript $(n+1)$ for the fluid forces and torques, is that these quantites are evaluated using the solid position at time t^{n+1} in the context of a time semi-implicit method (in contrast with [22] dealing with a rigid solid). The detailed procedure to compute the fluid forces and torques is described in Section 3.3.

3.2. Reconstruction of the deformed solid boundary

In Discrete Element method, the particles can overlap or become separated by small gaps as the solid is compressed or stretched, see Fig. 2. However, no fluid should penetrate into the gaps between the particles since the solid is treated here as cohesive. Therefore, we reconstruct a continuous interface around the particle assembly, as close as possible to the actual boundary of the moving particles.
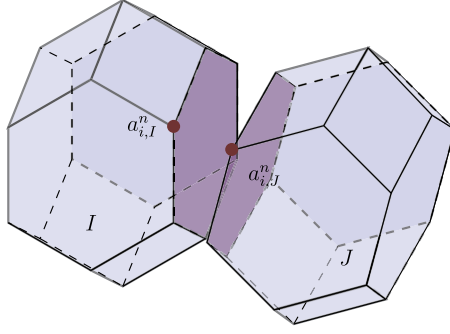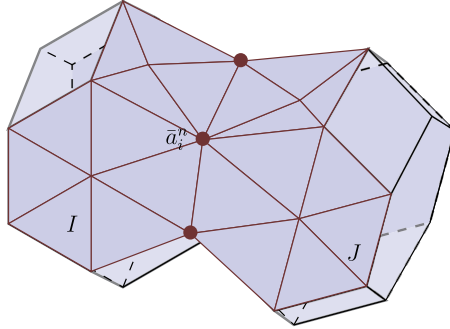
Fig. 2. Solid deformation.

Fig. 3. Reconstruction of the deformed solid boundary.

Several choices are possible for the reconstruction. For the sake of simplicity, we focus here on one simple option: the interface is reconstructed as a set of triangles with vertices obtained from a transformation of the vertices of the Discrete Elements lattice at time $t^0 = 0$. Since the faces of the particles are star-shaped with respect to their center of mass, we subdivide all the solid faces into triangles, by connecting the center of mass of the face to all the face vertices. Let us consider a vertex a_i of the initial Discrete Element lattice: it belongs to one or more polyhedral particles. Let us denote by $\mathcal{P}_{a_i}$ the set of particles which share the vertex a_i and by $\#\mathcal{P}_{a_i}$ the cardinality of the set $\mathcal{P}_{a_i}$. We define the mean vertex $\bar{a}_i^n$ corresponding to a_i at time t^n as the average of the positions of vertex a_i under the rigid body motion of each particle in $\mathcal{P}_{a_i}$:

$$\bar{a}_i^n = \frac{1}{\#\mathcal{P}_{a_i}} \sum_{J \in \mathcal{P}_{a_i}} (X_J^n + \mathbf{Q}_J^n \cdot (a_i^0 - X_J^0)), \tag{18}$$

where a_i^0 is the initial position of a_i. The reconstructed fluid–solid interface at time t^n is the set of triangles supported by the center of mass of the polyhedral particle faces and the mean vertices $(\bar{a}_i^n)_i$. This procedure is applied to all the vertices belonging to a polyhedral face of the Discrete Elements in contact with the fluid. A typical boundary reconstruction is shown in Fig. 3. Note that owing to the above reconstruction, the area of a wet solid face becomes time-dependent.

3.3. Evaluation of the fluid pressure forces

Owing to the deformation of the solid, the surface of the wet solid face $\mathcal{F}(t)$ evolves during the time-step. The following geometric conservation laws in the cell $C_{i,j,k}$ play an important role in the consistency properties of the coupling method:

$$\lambda_{i+\frac{1}{2},j,k}^{n+1} = \lambda_{i-\frac{1}{2},j,k}^{n+1} - \sum_{\{\mathcal{F} \in \mathfrak{F} \,|\, \mathcal{F}^{n+1} \cap C_{i,j,k} \neq \emptyset\}} \frac{A_{i,j,k,\mathcal{F}}^{n+1}}{\Delta y_{i,j,k} \, \Delta z_{i,j,k}} v_{x,\mathcal{F}}^{n+1}, \tag{19}$$

$$\lambda_{i,j+\frac{1}{2},k}^{n+1} = \lambda_{i,j-\frac{1}{2},k}^{n+1} - \sum_{\{\mathcal{F} \in \mathfrak{F} \,|\, \mathcal{F}^{n+1} \cap C_{i,j,k} \neq \emptyset\}} \frac{A_{i,j,k,\mathcal{F}}^{n+1}}{\Delta x_{i,j,k} \, \Delta z_{i,j,k}} v_{y,\mathcal{F}}^{n+1}, \tag{20}$$

$$\lambda_{i,j,k+\frac{1}{2}}^{n+1} = \lambda_{i,j,k-\frac{1}{2}}^{n+1} - \sum_{\{\mathcal{F} \in \mathfrak{F} \,|\, \mathcal{F}^{n+1} \cap C_{i,j,k} \neq \emptyset\}} \frac{A_{i,j,k,\mathcal{F}}^{n+1}}{\Delta x_{i,j,k} \, \Delta y_{i,j,k}} v_{z,\mathcal{F}}^{n+1}, \tag{21}$$

recalling that $\lambda_{i\pm\frac{1}{2},j,k}$, $\lambda_{i,j\pm\frac{1}{2},k}$, and $\lambda_{i,j,k\pm\frac{1}{2}}$ are the side area fractions of the fluid cell $C_{i,j,k}$ faces. Conditions (19), (20), and (21) can be satisfied exactly by taking the position at time t^{n+1} of the wet solid face $\mathcal{F}(t)$. This is the reason why we consider $A_{\mathcal{F}}^{n+1}$ and $\vec{v}_{\mathcal{F}}^{n+1}$. Such a choice in turn requires to solve the solid with a time-implicit algorithm which could be computationally expensive. We choose a time semi-implicit algorithm which only computes implicitly the position of particles in contact with the fluid by means of an iterative procedure. Moreover, we compute the internal forces between particles only once, since this is the most time-demanding step of the Discrete Element method. This computation is based on the position of particles at time t^n, and the internal forces are then kept fixed in the iterative procedure employed by the time semi-implicit algorithm. In the same way, the fluid pressure has already been computed and remains fixed during the iterative procedure. For the solid particles in contact with the fluid, we employ an additional index k within the iterative procedure. We compute the forces exerted by the fluid pressure on the surface $A_{\mathcal{F}}^{n,k}$, advance the position of the solid particles having wet faces, while the internal and external pressure forces are kept fixed. We can then update the surface $A_{\mathcal{F}}^{n,k+1}$ and the normal $\vec{v}_{\mathcal{F}}^{n,k+1}$. We iterate the process until convergence. As a result, the fluid force acting on the wet solid face $\mathcal{F}^{n+1}$ is evaluated using the boundary area $A_{\mathcal{F}}^{n+1}$.

We observe that the time-explicit variant (one step in the iterative procedure) in which we take the position at time t^n of the solid wet face $\mathcal{F}(t)$, so that we consider $A_{\mathcal{F}}^n$ and $\vec{v}_{\mathcal{F}}^n$ for the evaluation of the fluid forces, is cheaper but loses some consistency properties because conditions (19), (20), and (21) are no longer satisfied exactly for a deformable solid. We therefore expect pressure fluctuations near a solid boundary deformed tangentially, whereas the slip boundary conditions should not yield such a behavior. A numerical illustration is presented in Section 4.2.

An important remark is that the above procedure is more efficient than a global time-implicit method. Indeed, the iterative procedure only involves the computation of the positions of the solid particles in contact with the fluid. In addition, the expensive computation of the solid internal forces, fluid fluxes, and swept amount are not carried out during the iterative loop: the only operations involved are the computation of fluid pressure forces, the increment of the particle positions, the computation of the intersection between the solid and the fluid grid cells, and the reconstruction of the solid boundary. Among these operations, the most computationally expensive is the computation of the intersection between the solid and the fluid grid. We assess the efficiency of the time semi-implicit method in Section 5. We also prove in Section 4.3 that under a classical CFL condition on the time-step, the above iterative procedure converges at a geometric rate.

3.4. Main steps of the time semi-implicit algorithm

At the beginning of the time step from t^n to t^{n+1}, we know the state of the fluid U^n, the position and rotation of the solid particles $(\vec{X}_I^n, \mathbf{Q}_I^n)$, as well as the velocity of their center of mass and their angular momentum $(\vec{V}_I^n, \mathbf{P}_I^n)$. For the fluid, we need to compute for all the fluid grid cells the fluxes $F^{n+\frac{1}{2}}, G^{n+\frac{1}{2}}, H^{n+\frac{1}{2}}$, the volume fractions Λ^{n+1} and the side area fractions λ^{n+1}, and the solid fluxes $\phi_{\mathcal{F}}^{n+1}$ and the swept amounts $\Delta U_{\mathcal{F}}^{n,n+1}$ for all the wet solid faces $\mathcal{F}$. For the solid, we need to compute the fluid forces and torques $\vec{F}_{I,\text{fluid}}^{n+1}$ and $\vec{\mathcal{M}}_{I,\text{fluid}}^{n+1}$ for all the solid particles I. Recalling the iterative procedure introduced in Section 3.3, we use the superscript k for all variables at the k-th step of this procedure. In particular, we denote by $\vec{F}_{I,\text{fluid}}^{n,k}$ and $\vec{\mathcal{M}}_{I,\text{fluid}}^{n,k}$ the fluid force and torque at time t^n and at the k-th step of the iterative procedure. The convergence criterion is

$$\max_I \|X_I^{n,k+1} - X_I^{n,k}\| + \max_I h_{s,I}\|\mathbf{Q}_I^{n,k+1} - \mathbf{Q}_I^{n,k}\| \leq \epsilon = 10^{-12}. \tag{22}$$

The general structure of the time semi-implicit method is summarized in Fig. 4 and can be described by the following seven steps:

1. The fluid fluxes $F^{n+\frac{1}{2}}, G^{n+\frac{1}{2}}, H^{n+\frac{1}{2}}$ used in (13) are precomputed at all the cell faces of the fluid grid, without taking into account the presence of the solid. We use the OSMP scheme with directional operator splitting. For instance,

$$U_{i,j,k}^{n+1} = L_x(\Delta t)L_y(\Delta t)L_z(\Delta t)\, U_{i,j,k}^n,$$

where L_x, L_y, L_z are respectively the operators corresponding to the integration of a time step Δt in the x, y and z directions. For instance,

$$L_x(\Delta t)W = W - \frac{\Delta t}{\Delta x}\left(F_{i+\frac{1}{2},j,k}(W) - F_{i-\frac{1}{2},j,k}(W)\right).$$

Thus, formal second-order time accuracy is recovered every six time steps (corresponding to all L_x, L_y, and L_z permutations) if the directional operators do not commute. We denote by $\bar{p}_x^n$, $\bar{p}_y^n$, and $\bar{p}_z^n$ the pressures used in the application of the operators L_x, L_y, and L_z respectively. These pressures are used to determine the forces exerted by the fluid on the solid in step (2).

2. The internal forces and torques are computed based on the position of the solid particles using (A.1) and (A.2).

3. The fluid pressure force acting on a solid particle I used in (14)–(17) is decomposed as:

$$\vec{F}_{I,\text{fluid}}^{n,k} = \sum_{\mathcal{F}\in\mathfrak{F}_I} \vec{F}_{\mathcal{F},\text{fluid}}^{n,k}, \tag{23}$$
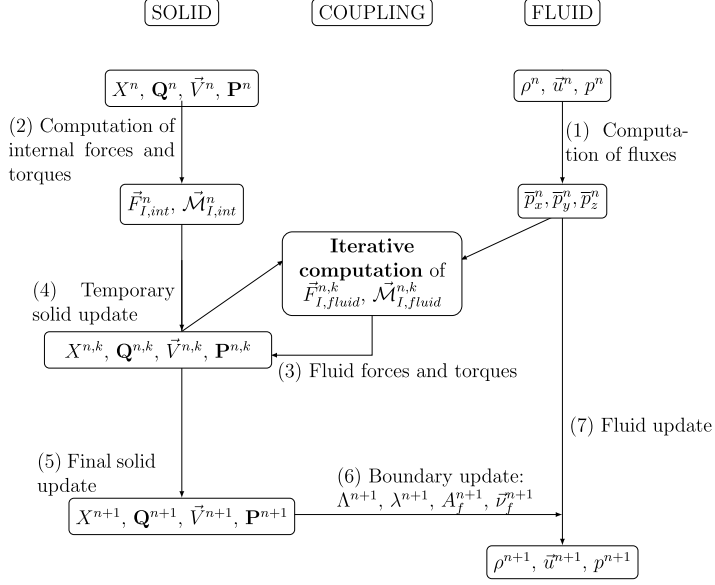
Fig. 4. Structure of the time semi-implicit scheme.

where $\mathfrak{F}_I$ collects the wet faces of the particle I, and the fluid force $\vec{F}^{n,k}_{\mathcal{F},\text{fluid}}$ acting on the wet solid face $\mathcal{F}^{n,k}$ is equal to the force exerted by the pressures $\bar{p}^n_x$, $\bar{p}^n_y$, and $\bar{p}^n_z$ on the surface in contact with the fluid:

$$
\vec{F}^{n,k}_{\mathcal{F},\text{fluid}} = \left(-\int_{\mathcal{F}^{n,k}} \bar{p}^n_x \nu^{n,k}_{x,\mathcal{F}}, \ -\int_{\mathcal{F}^{n,k}} \bar{p}^n_y \nu^{n,k}_{y,\mathcal{F}}, \ -\int_{\mathcal{F}^{n,k}} \bar{p}^n_z \nu^{n,k}_{z,\mathcal{F}} \right)^t .
\tag{24}
$$

Similarly, the fluid torque $\vec{\mathcal{M}}^{n,k}_{I,\text{fluid}}$ is decomposed as

$$
\vec{\mathcal{M}}^{n,k}_{I,\text{fluid}} = \sum_{\mathcal{F} \in \mathfrak{F}_I} \vec{F}^{n,k}_{\mathcal{F},\text{fluid}} \wedge (\vec{X}^{n,k}_{\mathcal{F}} - X^{n,k}_I),
\tag{25}
$$

where $\vec{X}^{n,k}_{\mathcal{F}}$ is the center of mass of the wet solid face $\mathcal{F}^{n,k}$ and $X^{n,k}_I$ the center of mass of the particle I at time $t^{n,k}$.

4. The solid is advanced in time. The position of each particle I is integrated using (5), (7), and (14)–(17). We obtain the temporary position of the center of mass $X^{n,k+1}_I$ and its velocity $\vec{V}^{n,k+1}_I$, the rotation matrix $\mathbf{Q}^{n,k+1}_I$, and the angular momentum matrix $\mathbf{P}^{n,k+1}_I$.

5. Iterate on steps (3) and (4) until convergence is reached using criterion (22).

6. The volume fractions Λ^{n+1} and side area fractions λ^{n+1} are computed using the final position of the fluid–solid interface. The fluid fluxes in (13) are modified using λ^{n+1}. At this stage, we also calculate the swept amount $\Delta U^{n,n+1}_{\mathcal{F}}$.

7. The final value of the state $U^{n+1}_{i,j,k}$ in the fluid grid cell is calculated using (12). Owing to the perfect slip conditions at the solid boundary, the solid flux $\phi^{n+1}_{\mathcal{F}}$ is given by

$$
\phi^{n+1}_{\mathcal{F}} = \left(0, \ \Pi^{n+1}_{x,\mathcal{F}}, \ \Pi^{n+1}_{y,\mathcal{F}}, \ \Pi^{n+1}_{z,\mathcal{F}}, \ \vec{V}^{n+\frac{1}{2}}_{\mathcal{F}} \cdot \vec{\Pi}^{n+1}_{\mathcal{F}} \right)^t,
\tag{26}
$$

where

$$
\vec{\Pi}^{n+1}_{\mathcal{F}} = \left(\int_{\mathcal{F}^{n+1}} \bar{p}^n_x \nu^{n+1}_{x,\mathcal{F}}, \ \int_{\mathcal{F}^{n+1}} \bar{p}^n_y \nu^{n+1}_{y,\mathcal{F}}, \ \int_{\mathcal{F}^{n+1}} \bar{p}^n_z \nu^{n+1}_{z,\mathcal{F}} \right)^t = -\vec{F}^{n+1}_{\mathcal{F},\text{fluid}},
$$

and $\vec{V}^{n+\frac{1}{2}}_{\mathcal{F}}$ is the velocity of the center of mass of the wet solid face $\mathcal{F}^{n+1}$:

$$
\vec{V}^{n+\frac{1}{2}}_{\mathcal{F}} = V^{n+\frac{1}{2}}_I + \vec{\Omega}^{n+\frac{1}{2}}_I \wedge (\vec{X}^{n+1}_{\mathcal{F}} - \vec{X}^{n+1}_I),
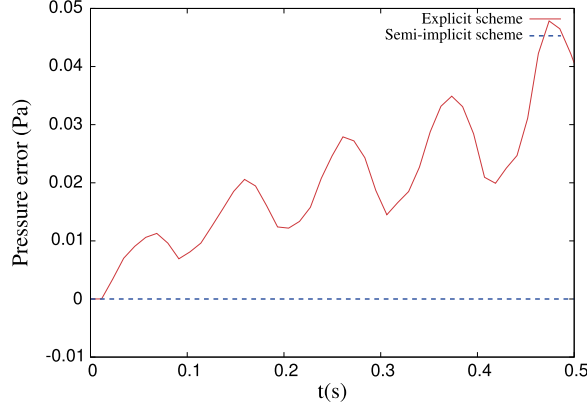$$

Fig. 5. Maximum pressure error as a function of time for the time-explicit and semi-implicit schemes.

where $V_I^{n+\frac{1}{2}}$ results from (14), and the angular velocity $\vec{\Omega}_I^{n+\frac{1}{2}}$ at time $(n+\frac{1}{2})\Delta t$ is defined from the relation

$$\mathbf{j}(\vec{\Omega}_I^{n+\frac{1}{2}}) = \frac{1}{2}\mathbf{P}_I^{n+\frac{1}{2}}\mathbf{D}_I^{-1}(\mathbf{Q}_I^n + \mathbf{Q}_I^{n+1})^t.$$

The most computationally expensive steps are steps (1), (2), and (6). The first two steps are independent. The rest of the procedure is localized on the fluid cells and solid particles in contact with the fluid–solid interface. The parallelization of the procedure with domain decomposition (in fluid and solid) has therefore the potential to be scalable. These aspects are not further explored herein.

4. Properties of the coupling scheme

4.1. Conservation of mass, momentum, and energy

Conservation of mass, momentum, and energy holds for periodic boundary conditions and more generally in all the cases where such properties hold at the continuous level. We refer to [21] and [26] for the proof in the rigid case; the proof in the case of a deformable solid is similar.

4.2. Consistency properties

- The coupling method preserves exactly a uniform constant flow parallel to a rigid half-space, even in the case where the fluid–solid interface is not aligned with the fluid grid. This result shows that no artificial roughness is produced by the solid walls.
- Consider an arbitrarily-shaped rigid body moving at constant velocity and without rotation, immersed in a uniform fluid flowing at the same velocity. Then, the uniform movement of the fluid and the solid is preserved by the coupling method.

We refer to [21] and [26] for the proof in the rigid case; the proof in the case of a deformable solid is similar.

Moreover, the coupling method preserves a constant fluid state around a wall having only tangential deformation velocity. This case is a prototypical example of the inconsistency of the time-explicit scheme (one step in the iterative procedure). In order to verify this property, we consider the following test case. A rod having a square section is immersed in a gas at constant state $(\rho, \vec{u}, p) = (1.4 \text{ kg m}^{-3}, \vec{0} \text{ m s}^{-1}, 1 \text{ Pa})$. The Young modulus and Poisson ratio of the rod are, respectively, $E = 7000$ Pa and $\nu = 0$. The rod is discretized with 4 square particles along its length. The two extremal particles are fixed, and the two other particles have an initial velocity $\vec{V} = 0.25\vec{e}_x$. The computation is carried out until $t = 0.5$ s. The rod exhibits internal deformations, with both ends remaining fixed. As the Poisson ratio is $\nu = 0$ and the force is directed along the axis of the rod, no normal deformation occurs at the surface of the rod. Only tangential deformations of the surface appear on the lateral sides of the rod. As shown in Fig. 5, the tangential deformation of the boundary creates pressure oscillations for the time-explicit scheme, whereas the time semi-implicit scheme preserves the constant fluid state. The error for the time-explicit scheme grows when the velocity of the particles is largest. On the contrary, the time semi-implicit scheme is able to eliminate totally the error (up to numerical rounding errors involved in the evaluation of geometric quantities in cut-cells and incomplete convergence of the fixed-point procedure).

4.3. Convergence for the time semi-implicit scheme

Let $\mathcal{F} \in \mathfrak{F}_I$ be a wet solid face of the particle I. We define the pressure $\bar{p}_{\mathcal{F}}^n = \max\{\bar{p}_x^n, \bar{p}_y^n, \bar{p}_z^n\}$ where the boundary pressures $\bar{p}_x^n$, $\bar{p}_y^n$ and $\bar{p}_x^n$ are defined in Step (1) of Section 3.4. Note that these pressures do not change during the fixed-point

procedure. Let $\sigma_{s,I}$ denote the radius of the largest inscribed sphere in particle I, and recall that $h_{s,I}$ denotes the diameter of the particle. We define the real function $x \mapsto K(x)$ as

$$K(x) = \frac{15}{8\pi}x + \frac{165(1+2C(x))}{16\pi}x^3, \quad C(x) = \sqrt{3 + \frac{1}{2}x^5}. \tag{27}$$

Then, our main result is that, for Δt satisfying the CFL condition

$$\forall I, \quad K\left(\frac{h_{s,I}}{\sigma_{s,I}}\right) \frac{\Delta t^2}{\sigma_{s,I}^2} \sum_{\mathcal{F} \in \mathfrak{F}_I} \frac{\bar{p}_{\mathcal{F}}^n}{\rho_{s,I}} < 1, \tag{28}$$

the iterative procedure in the time semi-implicit scheme converges at a geometric rate. The proof is stated in Appendix B.

Let us comment on condition (28). For a given aspect ratio $\frac{h_{s,I}}{\sigma_{s,I}}$ of the solid particles, the upper bound on the time step Δt resulting from (28) is proportional to the maximal diameter of the solid particles $h_{s,I}$. Moreover, the constant involves the ratio $\frac{\bar{p}_{\mathcal{F}}^n}{\rho_s}$: if the solid density is assumed to be larger than the fluid density (which is the case in our intended applications), $\frac{\bar{p}_{\mathcal{F}}^n}{\rho_s}$ is less than the square of the maximal sound celerity of the fluid c^2. Condition (28) is compatible with the stability results found in [27]: a very small solid density induces numerical instabilities of the overall explicit coupling strategy. As our bounds are expected to be rather pessimistic, condition (28) is in practice less restrictive than the fluid CFL condition. We have verified this assertion on numerous simulations, in which the iterative procedure always converged in less than 7 iterations without explicitly enforcing (28).

5. Numerical results

In this section we present numerical results. We first consider the interaction of a shock wave with a two- and three-dimensional clamped beam. Then, we simulate the effect of an explosion on a steel cylinder in two space dimensions. Finally, we consider the interaction of a shock wave with a two-dimensional deformable thin shell.

5.1. Clamped beam

5.1.1. 2d clamped beam

Consider a 4 m long and 2 m large channel with fixed reflecting bottom and top solid boundaries. Periodic boundary conditions are applied to both ends of the channel. Initially, the gas in the channel forms a double shock tube: the states are $(\rho, \vec{u}, p) = (8 \text{ kg m}^{-3}, \vec{0} \text{ m s}^{-1}, 116.5 \text{ Pa})$ for $0 < x < 1.5$ m, and $(\rho, \vec{u}, p) = (1.4 \text{ kg m}^{-3}, \vec{0} \text{ m s}^{-1}, 1 \text{ Pa})$ for $1.5 \text{ m} < x < 4$ m. The fluid domain is discretized with 400×200 elements ($\Delta x = \Delta y = 10^{-2}$ m). A beam is clamped at the bottom of the channel, its center is located at $x = 2$ m. The beam is 0.2857 m wide and 1 m long. The beam density and Young modulus of the beam are, respectively, $\rho_s = 100 \text{ kg m}^{-3}$ and $E = 7000$ Pa, with a Poisson ratio $\nu = 0$. The beam is discretized with 14×50 square particles ($h_s = 2 \times 10^{-2}$ m).

In Fig. 6, we show the normal stress in the beam and the pressure profile in the fluid at time $t = 0.08$ s. On the left of the beam, we observe the primary reflected shock followed by successive compression waves induced by the multiple reflections of the shock wave inside the beam.

In Fig. 7, we present the relative energy conservation error, computed as the difference between the initial energy and the discrete energy normalized by the maximum energy exchange between the fluid and the solid (which is the relevant quantity to evaluate the relative effect of coupling on conservation issues). We observe a small variation of energy, without any clear growth or decrease. The variation of energy is as low as 0.01% of the energy exchange in the system. This fluctuation of energy is not linked to the convergence criterion, but originates from the fluctuation of the discrete energy in the symplectic scheme. However, we observe no energy drift during the simulation. Fig. 7 also presents the same result with refined time steps $\Delta t/2$ and $\Delta t/4$. As expected, the energy conservation error decreases to zero with the time step, with second-order accuracy. This shows that the present coupling method ensures a long-term energy conservation of the system in the case of a deformable solid.
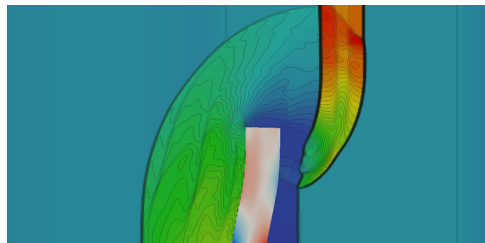

Fig. 6. Normal stress in the beam and the time evolution of the pressure profile in the fluid at time $t = 0.08$ s (50 contours in the fluid from 0 to 160 Pa).
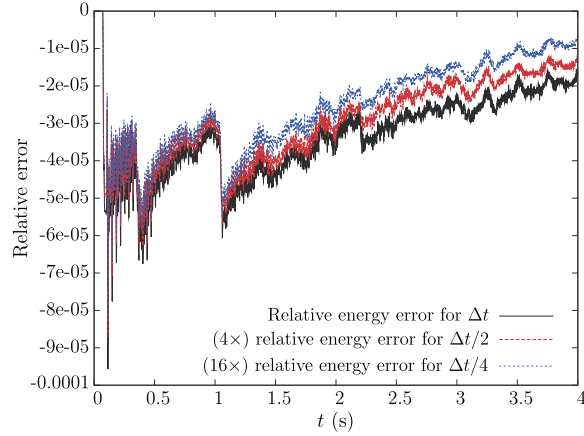
Fig. 7. Relative energy conservation error as a function of time for time-steps Δt, $\Delta t/2$ (rescaled by a factor 4) and $\Delta t/4$ (rescaled by a factor 16).
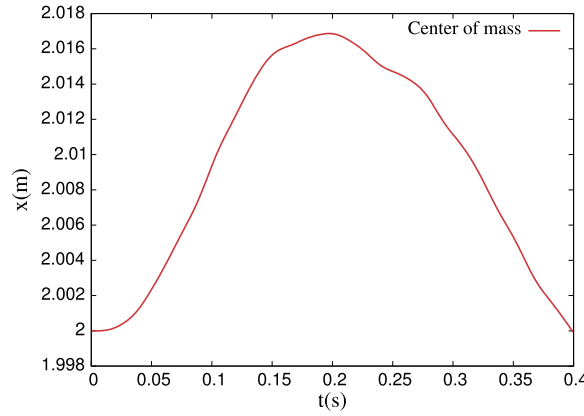

Fig. 8. x-Coordinate of the center of mass of the particle situated at the top of the beam as a function of time.

5.1.2. 3d clamped beam

Consider a 4 m long, 2 m large, and 2 m deep channel. Periodic boundary conditions are applied to both ends of the channel. Initially, the gas in the channel forms a double shock tube: the state is $(\rho, \vec{u}, p) = (8 \text{ kg m}^{-3}, \vec{0} \text{ m s}^{-1}, 116.5 \text{ Pa})$ for $0 < x < 1.5$ m, and $(\rho, \vec{u}, p) = (1.4 \text{ kg m}^{-3}, \vec{0} \text{ m s}^{-1}, 1 \text{ Pa})$ for $1.5 \text{ m} < x < 4$ m. The fluid domain is discretized with $100 \times 50 \times 50$ elements ($\Delta x = \Delta y = \Delta z = 0.04$ m). The beam is 0.2857 m wide, 1 m long, and 0.2857 m high. The beam is clamped at the bottom of the channel, its center is located at ($x = 2$ m, $y = 0$ m, $z = 1$ m). The density, Young modulus, and the Poisson ratio of the beam are identical as in the two-dimensional case. The beam is discretized with 24 tetrahedral particles ($h_x = 0.2857$ m, $h_y = 0.1428$ m, $h_z = 0.2857$ m).

In Fig. 8, we show the x-coordinate of the center of mass of the particle situated at the top of the beam during the simulation. In Fig. 9, we show the trajectory of the same point in the xy-plane. We observe that the x-coordinate advances during 0.2 s from 2 m to 2.0165 m and returns quite close to the initial position after the same lapse of time. Indeed, the beam undergoes a quasi-periodic motion composed of various vibration modes (the main one being the first flexure mode), partially damped by the interaction with the fluid and also perturbed by the development of multiple waves within the periodic domain.

In Fig. 10, we present the relative energy conservation error, computed as the difference between the initial energy and the energy computed at the different time steps. This energy difference is normalized by the maximum energy exchange between the fluid and the solid. We observe a small variation of relative energy, without any clear growth or decrease, as low as 0.03%. Thus, the same conclusions can be drawn as in the two-dimensional case.

5.2. Deformation of a cylinder filled with gas

In this test case, we simulate the effect of an explosion on a shell formed by a steel cylinder in two space dimensions. The cylinder is initially surrounded by gas at atmospheric pressure and contains gas at 0.1 bar. An overpressure region is initiated in the vicinity of the cylinder resulting in shock waves hitting the solid. This test case is designed to show the
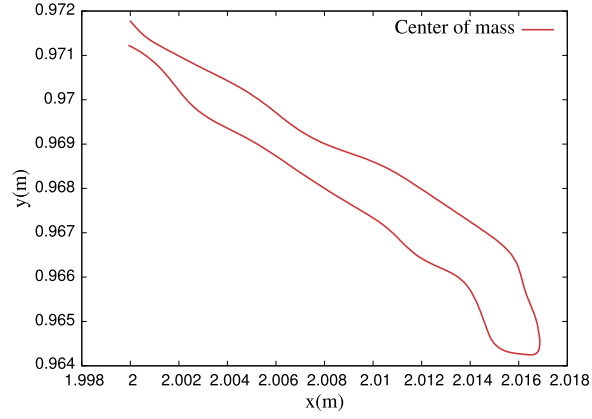
Fig. 9. Trajectory of the center of mass of the particle situated at the top of the beam in the xy-plane.
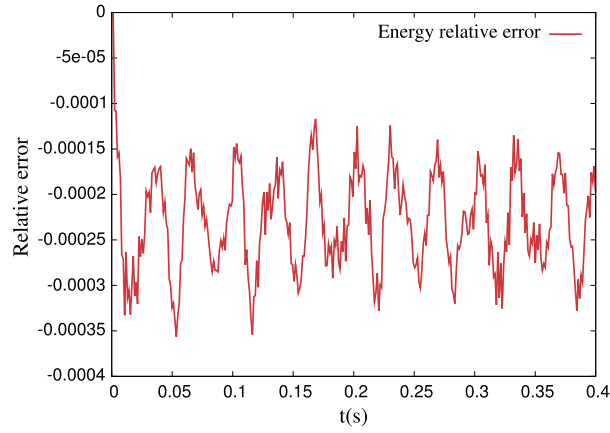

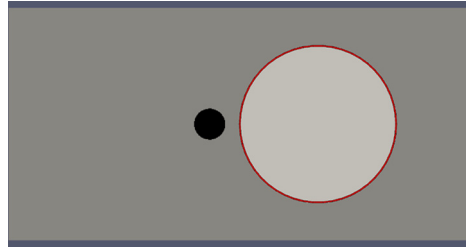**Fig. 10.** Relative energy conservation error as a function of time.

Fig. 11. Density profile in the fluid and cylinder position at time $t = 0$ s.

ability of the coupling scheme to handle physically relevant parameters and to give insight into the effect of shock waves on tubes filled with gas. This test case is a first step towards rupture test cases in three space dimensions.

The computational domain is the box $[0, 30] \times [0, 15]$ m. The boundaries of the domain are outflow boundaries with Poinsot–Lele boundary conditions [28]. Initially, the state of the gas is:

$$\begin{cases} \rho = 1.18 \text{ kg m}^{-3},\ \vec{u} = \vec{0} \text{ m s}^{-1},\ p = 101325 \text{ Pa, if } (x, y) \in D((20, 7.5), 5.1) \text{ m}, \\ \rho = 99.93 \text{ kg m}^{-3},\ \vec{u} = \vec{0} \text{ m s}^{-1},\ p = 50662500 \text{ Pa, if } (x, y) \in D((13, 7.5), 1) \text{ m} \\ \rho = 0.118 \text{ kg m}^{-3},\ \vec{u} = \vec{0} \text{ m s}^{-1},\ p = 10132.5 \text{ Pa, otherwise} \end{cases}$$

where $D((x_0, y_0), R)$ denotes the disk centered at (x_0, y_0) with radius R. The computation is performed on a 800×400 grid. The cylinder is centered at $(20, 7.5)$ m with a thickness of 0.1 m and an interior radius of 5 m. The density and the Young modulus are, respectively, $\rho_s = 7860$ kg m^{-3} and $E = 210$ Pa, with a Poisson ratio $\nu = 0$. The cylinder is discretized with 50 particles along its circumference and 1 particle in thickness. The simulation time is $t = 0.0244$ s. In Fig. 11, we display the initial density field of the fluid and the initial position of the cylinder.
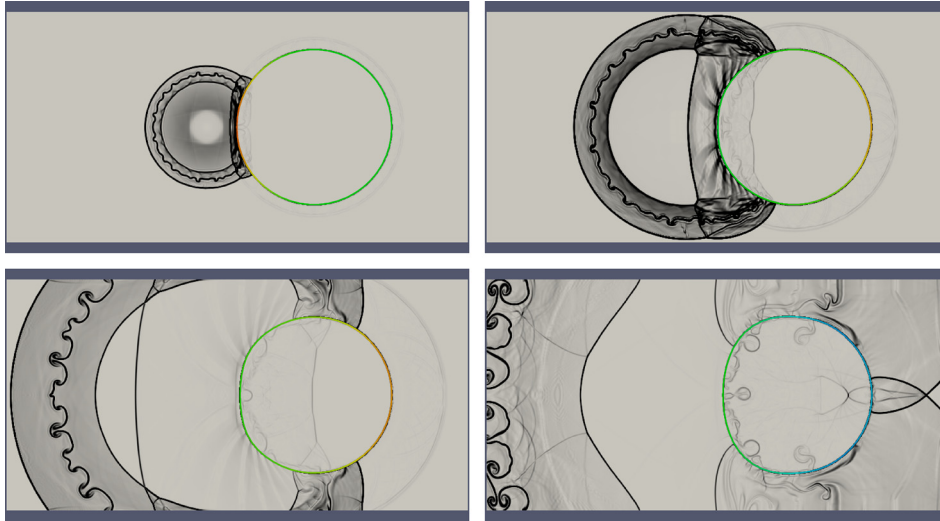
Fig. 12. Density gradient in the fluid and normal stress distribution in the cylinder at four times: 2×10^{-3} s, 4.7×10^{-3} s, 1×10^{-2} s, and 2.44×10^{-2} s from left to right and top to bottom.
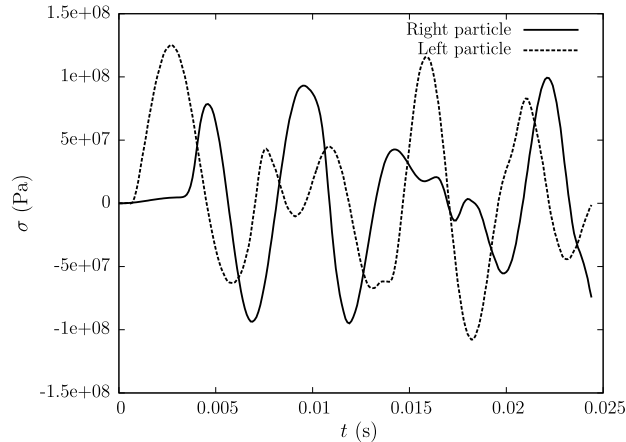

Fig. 13. Normal stress profile in the solid particle closest to the explosion (left particle) and in the solid particle farthest to the explosion (right particle) as a function of time.

After impacting the cylinder, the shock wave partially reflects on the solid and is partially transmitted by the solid to the confined underpressured gas. At the same time, the cylinder is deformed and pressure waves travel along its surface. We observe that the normal stress waves in the solid travel faster than those in the outer fluid, which in turn travel faster than those in the interior fluid due to the difference in pressures between the inside and the outside of the cylinder. In Fig. 12, we show the density field and the deformation of the solid at times 2×10^{-3} s, 4.7×10^{-3} s, 1×10^{-2} s, and 2.44×10^{-2} s. The circular rarefaction wave shed by the solid is caused by the difference of pressure between the inner and outer field, as the cylinder is not initially at equilibrium. We observe a Richtmyer–Meshkov instability of the contact discontinuity. The cylinder is flattened in the region first impacted by the fluid shock waves. However, the traction inside the solid reaches a maximum at the point opposite to the explosion, due to interactions between the solid normal stress waves. We guess that this point would be at the highest risk of rupture. Indeed, in Fig. 13, we display the normal stress in the solid particle closest to the explosion and in the solid particle farthest to the explosion in the course of the simulation. We observe, for both particles, an initial increase of normal stress (compression) due to the impact of the explosion, followed by negative normal stress (traction) due to the relaxation of the solid after impact. Complex interaction between the travelling waves on the surface of the cylinder and the fluid then occur, accounting for successive compression and traction phenomena at both ends of the cylinder. In Fig. 14, we display the displacement of the center of mass of the solid particle closest to the explosion and of the solid particle farthest to the explosion as function of time. We observe that the displacement of the solid particle farthest to the explosion is very small, whereas that of the solid particle closest to the explosion is large. This accounts for the flattening of the cylinder near the explosion impact.
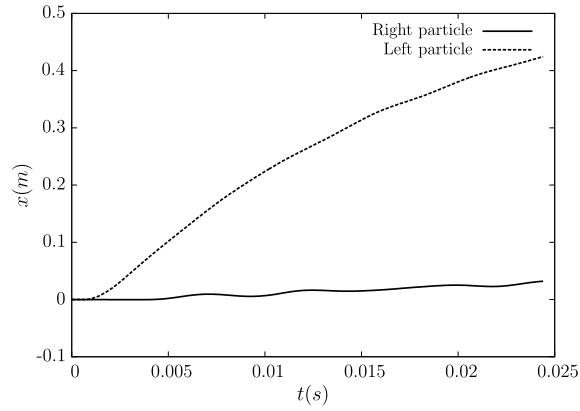
Fig. 14. *x*-coordinate of the center of mass of the solid particle closest to the explosion (left particle) and of the solid particle farthest to the explosion (right particle) as a function of time.
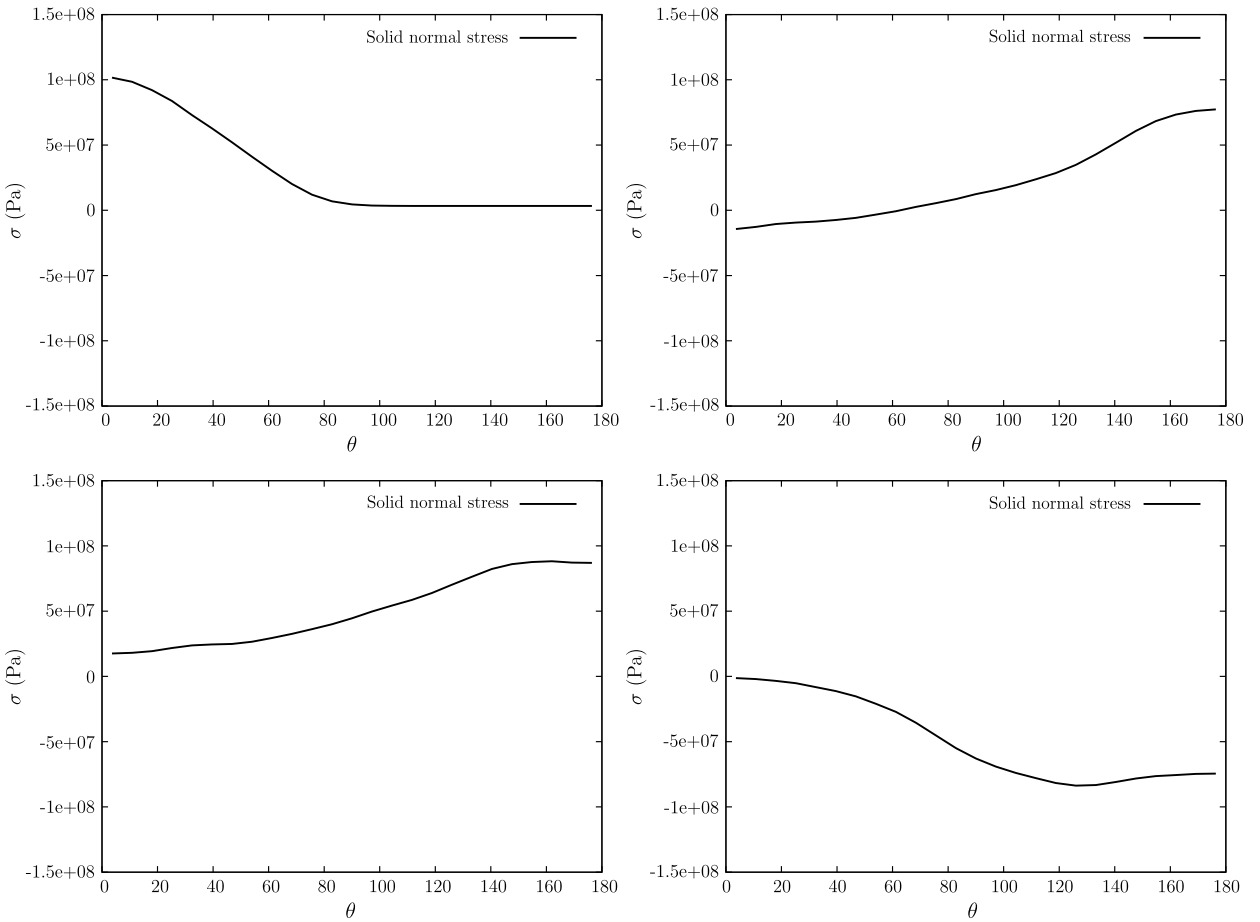

Fig. 15. Normal stress profile in the cylinder as a function of azimuthal angle at four times: 2×10^{-3} s, 4.7×10^{-3} s, 1×10^{-2} s, and 2.44×10^{-2} s from left to right and top to bottom.

In Fig. 15, we present the normal stress in the cylinder at times 2×10^{-3} s, 4.7×10^{-3} s, 1×10^{-2} s, and 2.44×10^{-2} s as a function of the azimuthal angle θ in polar coordinates. At time 2×10^{-3}, we observe the overpressure initiated by the impacting shock wave. At time 4.7×10^{-3}, we observe the interaction at the right tip of the cylinder of the two normal stress waves travelling along the upper and lower parts of the cylinder. The profiles at the two other times result from increasingly complex interactions between pressure waves. We observe that all the solid particles evolve between compression and traction states. The normal stress patterns are symmetric with respect to $\theta = 0$ owing to the symmetry
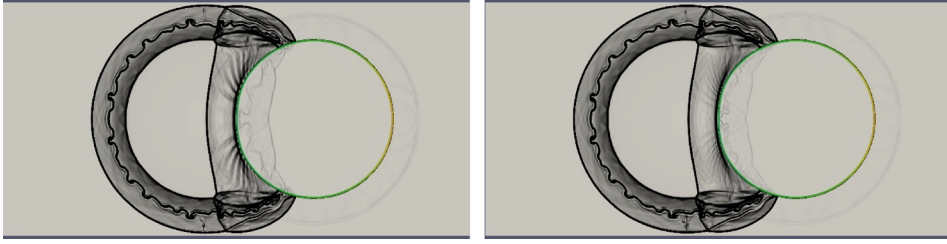
Fig. 16. Density gradient in the fluid and normal stress distribution in the cylinder at time 4.7×10^{-3} s for 100 solid particles (left) and 200 solid particles (right).
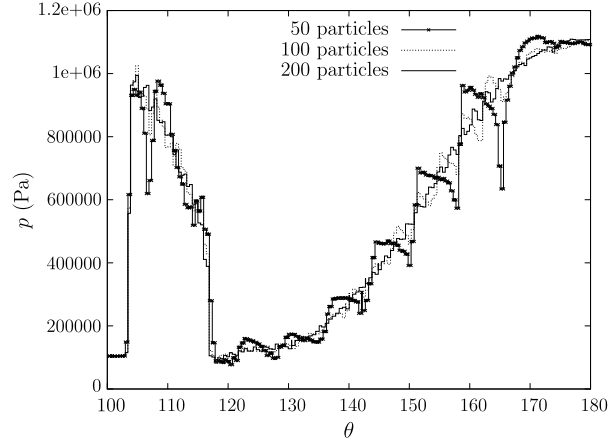

Fig. 17. Fluid pressure distribution along the cylinder at time 4.7×10^{-3} s for 50, 100, and 200 solid particles.

of the problem with respect to $y = 7.5$ m. We observe a sequence of rarefaction waves in the vicinity of the cylinder at time 4.7×10^{-3} s in Fig. 12. This phenomenon is directly related to the solid discretization: each edge of the polygon approximating the circle generates a rarefaction wave in the fluid flow around the cylinder. Refining the solid discretization to 100 and 200 solid particles along the cylinder perimeter, we observe in Fig. 16 that the number of rarefaction waves increases as the discretization is refined. The fluid pressure profile as a function of the azimuthal angle θ displayed in Fig. 17 shows that the intensity of each rarefaction wave decreases as the solid discretization is refined. Let us note that the pressure jumps occur exactly at the edge of the solid particles. Apart from these local discrepancies, the pattern of the fluid flow structures does not change significantly as the solid is refined.

5.3. Deformable thin shell

In this test case, we consider the interaction of a shock wave with a two-dimensional deformable thin shell. This benchmark was first simulated in [20]. The computational domain is the rectangular box $[0, 1] \times [0, 0.2]$ m and is discretized using a 640×128 grid. The shock is initially set up to a Mach number of 3, so that the initial values are

$$\begin{cases} \rho = 3.85 \text{ kg m}^{-3}, \ p = 10.33 \text{ Pa}, \ u = 2.69 \text{ m s}^{-1}, \ v = 0 \text{ m s}^{-1}, & x < 0.475 \text{ m}, \\ \rho = 1 \text{ kg m}^{-3}, \ p = 1 \text{ Pa}, \ \vec{u} = \vec{0} \text{ m s}^{-1}, & x \geq 0.475 \text{ m}. \end{cases}$$

The thin shell is placed at $x = 0.5$ m and its length is 0.1 m. The thin shell has a density of $\rho_s = 0.0238$ kg m^{-3} and the solid particles links have a stiffness of $k = 2000$ N m^{-1}. The thin shell is discretized with 20 particles. The two extremal particles are fixed. The simulation time is $t = 0.35$ s.

The impinging shock wave impacts the thin shell and is partially reflected to the left, while part of the shock wave moves over the thin shell and part of its energy is transferred as kinetic energy. At the same time, the thin shell is deformed due to the increase in pressure resulting in compression waves created by the movement of the thin shell. Complex interactions of waves occur due to solid movements and interaction with walls.

In Fig. 18, we show the density field and the deformation of the thin shell at times 0.07 s, 0.14 s, 0.21 s, 0.28 s, and 0.35 s. Our results are in very good agreement with [20] (Fig. 34) on the position of the solid and of the shocks (we use a four times coarser fluid grid, and the thin shell is discretized with the same number of particles).
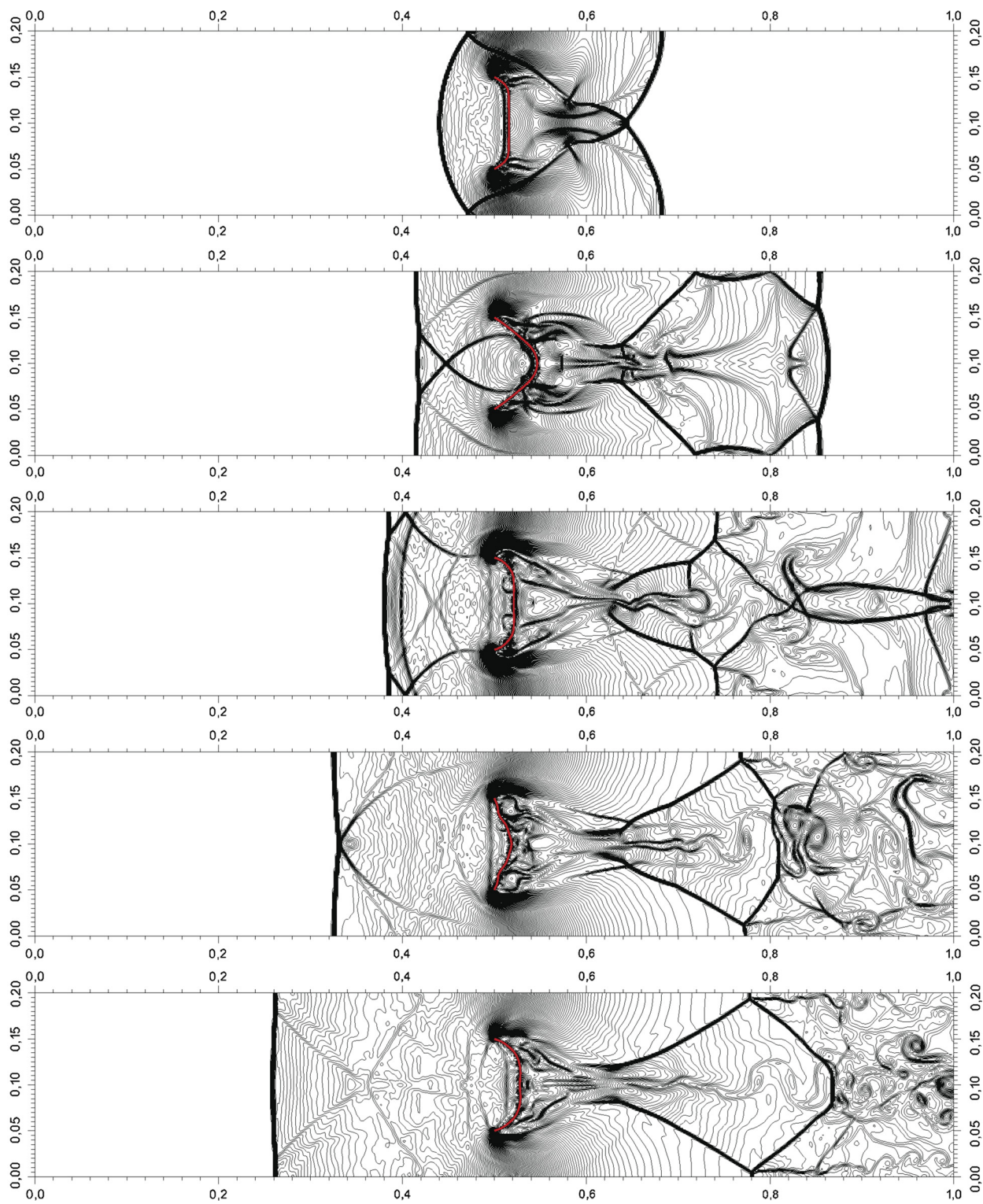
Fig. 18. Density field in the fluid and solid deformation at five times: 0.07 s, 0.14 s, 0.21 s, 0.28 s, and 0.35 s from top to bottom.

6. Conclusion

In this work, we have developed a coupling method for the interaction between a three-dimensional inviscid compressible fluid flow and a deformable structure undergoing large displacements. The method hinges on a cut-cell Finite Volume method for the fluid and a symplectic Discrete Element method for the deformable solid. The coupling method is exactly mass-conservative and exhibits a long-time preservation of the energy for the coupled system. Moreover, the coupling is handled in a time semi-implicit fashion. The computational cost of the fluid and solid methods essentially results from the evaluation of fluxes on the fluid side and of forces and torques on the solid side. We emphasize that the coupling algorithm evaluates these only once per time step, ensuring computational efficiency. Regarding surface coupling, the algorithm overhead scales as the number of solid faces and as $N^{\frac{2}{3}}$, N being the number of fluid grid cells. In comparison, the fluid flux computation time scales as N.

The presented test cases allowed us to verify the main properties of the coupling scheme and to illustrate the robustness of the method in the case of two- and three-dimensional deformable solids with large displacements coupled to an inviscid compressible flow. The next step is to move on to more complex test cases and to enrich the modelling to take into account the possible fragmentation of the solid. This would require an adequate reconstruction of the solid boundary, an appropriate procedure to fill the ghost-cells, and the definition of a map (not necessarily bijective due to the possible opening of fractures) providing the correspondence from the position of the boundary at time t^n to its position at time t^{n+1}. These developments are the subject of ongoing work.

Appendix A. The Discrete Element method

This appendix provides some background on the Discrete Element method. The set of neighbouring particles linked to particle I is denoted by τ_I. For each link between the particle I and a neighbouring particle $J \in \tau_I$, we denote by D_{IJ} the distance between these particles and by S_{IJ} the contact surface, see Fig. 19. Let G_{IJ}, $\vec{n}_{IJ}$, I^s_{IJ}, and I^t_{IJ} be the center of mass, the exterior normal vector, and the principal moments of the contact surface. Two orthogonal vectors are defined at the contact surface, $\vec{s}_{IJ}$ and $\vec{t}_{IJ}$, forming an orthonormal basis with $\vec{n}_{IJ}$. The initial values of these quantities are denoted with the superscript 0.

The forces and torques between particles are derived from a Hamiltonian formulation and are designed in order to recover at the macroscopic level a linear elasticity behavior [24,25]. We denote by E the Young modulus and by ν the Poisson ratio. The force between particles I and $J \in \tau_I$ is given by

$$\vec{F}_{IJ} = \vec{F}^n_{IJ} + \vec{F}^v_{IJ}, \tag{A.1}$$

where $\vec{F}^n_{IJ}$ is the shear and compression force and $\vec{F}^v_{IJ}$ the volumetric deformation force. The shear and compression force is given by

$$\vec{F}^n_{IJ} = \frac{S_{IJ}}{D^0_{IJ}} \frac{E}{1+\nu} \vec{\Delta u}_{IJ},$$

where $\vec{\Delta u}_{IJ} = X_I - X_J + \mathbf{Q}_J \cdot (G_{IJ} - X^0_J) - \mathbf{Q}_I \cdot (G_{IJ} - X^0_I)$ is the displacement vector to the contact surface between I and J. The volumetric deformation force is given by
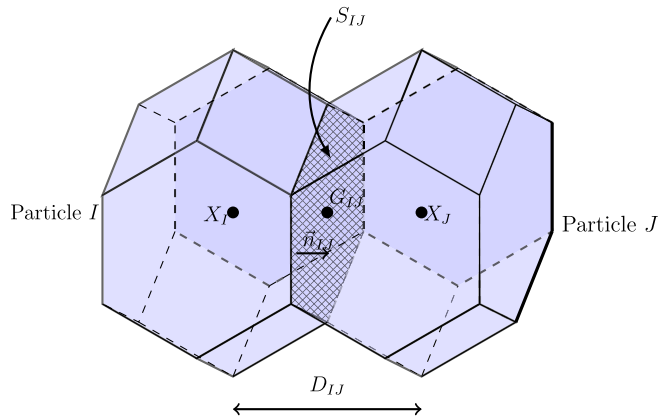

Fig. 19. Contact surface between particles.

$$\vec{F}_{IJ}^v = S_{IJ} \frac{E\nu}{(1+\nu)(1-2\nu)} \varepsilon_{IJ}^v \left(\vec{n}_{IJ} + \frac{1}{D_{IJ}} \vec{\Delta}u_{IJ} - \frac{1}{D_{IJ}} (\vec{\Delta}u_{IJ} \cdot \vec{n}_{IJ})\vec{n}_{IJ} \right),$$

where the volumetric deformation of the link between I and J, $\varepsilon_{IJ}^v = \varepsilon_I^v + \varepsilon_J^v$, is the sum of the volumetric deformation of I and J, where

$$\varepsilon_I^v = \sum_{J \in \tau_I} \frac{1}{2} \frac{S_{IJ}}{V_I + 3\frac{\nu}{1-2\nu}V_I^f} \vec{\Delta}u_{IJ} \cdot \vec{n}_{IJ},$$

where V_I and V_I^f are the volume and the free volume of the particle I, respectively. The free volume of the particle I is defined as the sum of the volumes of all pyramidal polyhedra with a free surface as basis and X_I^0 as summit.

The torque between particles I and J is expressed as

$$\vec{\mathcal{M}}_{IJ} = \vec{\mathcal{M}}_{IJ}^t + \vec{\mathcal{M}}_{IJ}^f, \tag{A.2}$$

where $\vec{\mathcal{M}}_{IJ}^t$ denotes the torque of force $\vec{F}_{IJ}$ and $\vec{\mathcal{M}}_{IJ}^f$ denotes the flexion–torsion torque. The torque of force $\vec{F}_{IJ}$ is given by

$$\vec{\mathcal{M}}_{IJ}^t = \frac{S_{IJ}}{D_{IJ}^0} \frac{E}{1+\nu} \left(\mathbf{Q}_I \cdot (G_{IJ} - X_I^0) \right) \wedge \vec{\Delta}u_{IJ} + S_{IJ} \frac{E\nu}{(1+\nu)(1-2\nu)} \varepsilon_{IJ}^v \left(\mathbf{Q}_I \cdot (G_{IJ} - X_I^0) \right) \wedge \vec{n}_{IJ}.$$

The flexion–torsion torque $\vec{\mathcal{M}}_{IJ}^f$ is given by

$$\vec{\mathcal{M}}_{IJ}^f = \frac{S_{IJ}}{D_{IJ}^0} (\alpha_n (\mathbf{Q}_I \cdot \vec{n}_{IJ}^0) \wedge (\mathbf{Q}_J \cdot \vec{n}_{IJ}^0) + \alpha_s (\mathbf{Q}_I \cdot \vec{s}_{IJ}) \wedge (\mathbf{Q}_J \cdot \vec{s}_{IJ}) + \alpha_t (\mathbf{Q}_I \cdot \vec{t}_{IJ}) \wedge (\mathbf{Q}_J \cdot \vec{t}_{IJ})).$$

The coefficients α_n, α_s, and α_t are chosen so as to recover the exact flexion and torsion of a beam. For a detailed review on the expression of these forces and torques between particles, see [21,24,25].

Appendix B. Convergence of the iterative procedure in the time semi-implicit scheme

This section is devoted to the proof of the convergence of the iterative procedure in the time semi-implicit scheme under the CFL condition (28). Let $(X^{n,k}, \mathbf{Q}^{n,k}) = \left((X_I^{n,k}, \mathbf{Q}_I^{n,k}) \right)_I$ be the geometric state vector collecting the position of the center of mass and the rotation matrix of the solid particles I at the k-th step of the iterative procedure described in Section 3.3. We consider the map χ such that $(X^{n,k+1}, \mathbf{Q}^{n,k+1}) = \chi(X^{n,k}, \mathbf{Q}^{n,k})$ denotes the state vector obtained at the $(k+1)$-th step. The map χ is defined more precisely in (B.13)–(B.14) below. We show that the map χ involved in the iterative procedure is contracting for the following norm:

$$\|(X, \mathbf{Q})\|_\infty = \max_I \|X_I\| + \max_I h_{s,I} \|\mathbf{Q}_I\|. \tag{B.1}$$

Here and in what follows, unless explicitly mentioned, the vector norm in $\mathbb{R}^3$ is the Euclidean norm, and the matrix norm is the induced spectral norm (i.e., the largest singular value of the matrix).

B.1. The map χ

The k-th step of the iterative procedure can be written as follows: For each particle I,

$$\vec{V}_I^{n,k+1} = \vec{V}_I^n + \frac{\Delta t}{2m_I} \left(\vec{F}_{I,\text{int}}^n + \vec{F}_{I,\text{fluid}}^{n,k} \right), \tag{B.2}$$

$$X_I^{n,k+1} = X_I^n + \Delta t \, \vec{V}_I^{n,k+1}, \tag{B.3}$$

$$\mathbf{P}_I^{n,k+1} = \mathbf{P}_I^n + \frac{\Delta t}{4} \mathbf{j}(\vec{\mathcal{M}}_{I,\text{int}}^n + \vec{\mathcal{M}}_{I,\text{fluid}}^{n,k})\mathbf{Q}_I^n + \frac{\Delta t}{2} \Upsilon_I^{n,k} \mathbf{Q}_I^n, \tag{B.4}$$

$$\mathbf{Q}_I^{n,k+1} = \mathbf{Q}_I^n + \Delta t \, \mathbf{P}_I^{n,k+1} \mathbf{D}_I^{-1}, \tag{B.5}$$

where $\vec{F}_{I,\text{int}}^n$ and $\vec{\mathcal{M}}_{I,\text{int}}^n$ denote the internal forces and torques on particle I at time t^n (which are independent of k) and $\vec{F}_{I,\text{fluid}}^{n,k}$ and $\vec{\mathcal{M}}_{I,\text{fluid}}^{n,k}$ denote the pressure forces and torques exerted by the fluid on particle I at time t^n and at the k-th step. We denote by $d_{\min,I}$ and $d_{\max,I}$, respectively, the smallest and largest eigenvalues of the matrix $\mathbf{D}_I$. Using the mass and inertia of a sphere of radius $\sigma_{s,I}$ and of the same density $\rho_{s,I}$ as the solid particle I, we obtain

$$m_I \geq \frac{4\pi}{3} \rho_{s,I} \sigma_{s,I}^3, \quad d_{\min,I} \geq \frac{4\pi}{15} \rho_{s,I} \sigma_{s,I}^5, \quad d_{\max,I} \leq \frac{4\pi}{15} \rho_{s,I} h_{s,I}^5. \tag{B.6}$$

Let $\mathcal{F}$ be a wet solid face and let I be the solid particle to which it belongs. As described in Section 3.2, the wet solid face is a triangle. We denote by a_1, a_2, and a_3 its vertices. We orient the triangle $\mathcal{F}$ for a given geometric state $(X, \mathbf{Q})$ of the solid by defining the surface and unit normal of $\mathcal{F}$ as

$$A_{\mathcal{F}}(X, \mathbf{Q}) \vec{v}_{\mathcal{F}}(X, \mathbf{Q}) = \frac{1}{2} (\bar{a}_2(X, \mathbf{Q}) - \bar{a}_1(X, \mathbf{Q})) \wedge (\bar{a}_3(X, \mathbf{Q}) - \bar{a}_1(X, \mathbf{Q})), \tag{B.7}$$

where we recall from (18) that the average position of the vertex $\bar{a}_i(X, \mathbf{Q})$ is given by

$$\bar{a}_i(X, \mathbf{Q}) = \frac{1}{\#\mathcal{P}_{a_i}} \sum_{J \in \mathcal{P}_{a_i}} (X_J + \mathbf{Q}_J \cdot (a_i^0 - X_J^0)), \tag{B.8}$$

where the superscript 0 refers to values at time $t^0 = 0$. We define the displacement $\vec{\xi}_a(X, \mathbf{Q})$ of a vertex a with respect to the geometric state at time t^n as follows:

$$\vec{\xi}_a(X, \mathbf{Q}) = \frac{1}{\#\mathcal{P}_a} \sum_{J \in \mathcal{P}_a} \left(X_J - X_J^n + (\mathbf{Q}_J - \mathbf{Q}_J^n) \cdot (a^0 - X_J^0) \right), \tag{B.9}$$

so that $\bar{a}(X, \mathbf{Q}) = \bar{a}^n + \vec{\xi}_a(X, \mathbf{Q})$. We define the fluid pressure force $\vec{F}_{I, \text{fluid}}(X, \mathbf{Q})$ on particle I as

$$\vec{F}_{I, \text{fluid}}(X, \mathbf{Q}) = \sum_{\mathcal{F} \in \mathfrak{F}_I} \vec{F}_{\mathcal{F}, \text{fluid}}(X, \mathbf{Q}), \quad \vec{F}_{\mathcal{F}, \text{fluid}}(X, \mathbf{Q}) = -\mathbf{P}_{\mathcal{F}}^n A_{\mathcal{F}}(X, \mathbf{Q}) \vec{v}_{\mathcal{F}}(X, \mathbf{Q}), \tag{B.10}$$

where $\mathbf{P}_{\mathcal{F}}^n = \text{diag}(\bar{p}_x^n, \bar{p}_y^n, \bar{p}_z^n)$. Using (B.7)–(B.10), the fluid pressure force is given by

$$\vec{F}_{\mathcal{F}, \text{fluid}}(X, \mathbf{Q}) = -\frac{1}{2} \mathbf{P}_{\mathcal{F}}^n \left[\left(\bar{a}_2^n - \bar{a}_1^n + \vec{\xi}_{a_2}(X, \mathbf{Q}) - \vec{\xi}_{a_1}(X, \mathbf{Q}) \right) \wedge \left(\bar{a}_3^n - \bar{a}_1^n + \vec{\xi}_{a_3}(X, \mathbf{Q}) - \vec{\xi}_{a_1}(X, \mathbf{Q}) \right) \right]. \tag{B.11}$$

Recall that the mean pressure on each wet solid face is constant during the iterative process. We define the fluid pressure torque $\vec{\mathcal{M}}_{I, \text{fluid}}(X, \mathbf{Q})$ on particle I as

$$\vec{\mathcal{M}}_{I, \text{fluid}}(X, \mathbf{Q}) = \sum_{\mathcal{F} \in \mathfrak{F}_I} \vec{F}_{\mathcal{F}, \text{fluid}}(X, \mathbf{Q}) \wedge (X_{\mathcal{F}}(X, \mathbf{Q}) - X_I), \tag{B.12}$$

where $X_{\mathcal{F}}(X, \mathbf{Q}) = X_{\mathcal{F}}^n + \frac{1}{3} \left(\vec{\xi}_{a_1}(X, \mathbf{Q}) + \vec{\xi}_{a_2}(X, \mathbf{Q}) + \vec{\xi}_{a_3}(X, \mathbf{Q}) \right)$ is the position of the center of mass of $\mathcal{F}^n$ for the solid geometric state $(X, \mathbf{Q})$. We set

$$\vec{C}_I^n = X_I^n + \Delta t \vec{V}_I^n + \frac{\Delta t^2}{2m_I} \vec{F}_{I, \text{int}}^n, \quad \Gamma_I^n = \mathbf{Q}_I^n + \Delta t \mathbf{P}_I^n \mathbf{D}_I^{-1} + \frac{\Delta t^2}{4} \mathbf{j}(\vec{\mathcal{M}}_{I, \text{int}}^n) \mathbf{Q}_I^n \mathbf{D}_I^{-1}.$$

Then, owing to (B.2)–(B.5), the map χ for a given geometric state $(X, \mathbf{Q})$ for the solid is given by $\chi(X, \mathbf{Q}) = ((\chi_{p,I}(X, \mathbf{Q}))_I, (\chi_{r,I}(X, \mathbf{Q}))_I)$ where

$$\chi_{p,I}(X, \mathbf{Q}) = \vec{C}_I^n + \frac{\Delta t^2}{2m_I} \sum_{\mathcal{F} \in \mathfrak{F}_I} \vec{F}_{\mathcal{F}, \text{fluid}}(X, \mathbf{Q}), \tag{B.13}$$

$$\chi_{r,I}(X, \mathbf{Q}) = \Gamma_I^n + \frac{\Delta t^2}{4} \left(\mathbf{j}(\vec{\mathcal{M}}_{I, \text{fluid}}(X, \mathbf{Q})) + 2 \Upsilon_I(X, \mathbf{Q}) \right) \mathbf{Q}_I^n \mathbf{D}_I^{-1}, \tag{B.14}$$

in such a way that $X_I^{n,k+1} = \chi_{p,I}(X^{n,k}, \mathbf{Q}^{n,k})$ and $\mathbf{Q}_I^{n,k+1} = \chi_{r,I}(X^{n,k}, \mathbf{Q}^{n,k})$.

B.2. Estimate on the position of the center of mass

Let $(X, \mathbf{Q})$ and $(Y, \mathbf{R})$ be two geometric states for the solid particles. Using the expression for $\vec{\xi}_a$ from (B.9) and the definition (B.1) of the $\| \cdot \|_\infty$-norm leads to

$$\| \vec{\xi}_a(X, \mathbf{Q}) - \vec{\xi}_a(Y, \mathbf{R}) \| \leq \| (X - Y, \mathbf{Q} - \mathbf{R}) \|_\infty. \tag{B.15}$$

Using the expression of the fluid pressure force from (B.11) together with the triangle inequality, and since $\| \mathbf{P}_{\mathcal{F}}^n \| = \bar{p}_{\mathcal{F}}^n$, we infer that

$$\| \vec{F}_{\mathcal{F}, \text{fluid}}(X, \mathbf{Q}) - \vec{F}_{\mathcal{F}, \text{fluid}}(Y, \mathbf{R}) \|$$
$$\leq \frac{\bar{p}_{\mathcal{F}}^n}{2} \left\{ \left\| (\bar{a}_2^n - \bar{a}_1^n) \wedge \left(\vec{\xi}_{a_3}(X, \mathbf{Q}) - \vec{\xi}_{a_3}(Y, \mathbf{R}) \right) \right\| + \left\| (\bar{a}_2^n - \bar{a}_1^n) \wedge \left(\vec{\xi}_{a_1}(X, \mathbf{Q}) - \vec{\xi}_{a_1}(Y, \mathbf{R}) \right) \right\| \right.$$
$$\left. + \left\| (\bar{a}_3^n - \bar{a}_1^n) \wedge \left(\vec{\xi}_{a_2}(X, \mathbf{Q}) - \vec{\xi}_{a_2}(Y, \mathbf{R}) \right) \right\| + \left\| (\bar{a}_3^n - \bar{a}_1^n) \wedge \left(\vec{\xi}_{a_1}(X, \mathbf{Q}) - \vec{\xi}_{a_1}(Y, \mathbf{R}) \right) \right\| \right.$$

$$+ \left\| \left(\vec{\xi}_{a_2}(X,\mathbf{Q}) - \vec{\xi}_{a_1}(X,\mathbf{Q})\right) \wedge \left(\vec{\xi}_{a_3}(X,\mathbf{Q}) - \vec{\xi}_{a_1}(X,\mathbf{Q})\right) - \left(\vec{\xi}_{a_2}(Y,\mathbf{R}) - \vec{\xi}_{a_1}(Y,\mathbf{R})\right) \wedge \left(\vec{\xi}_{a_3}(Y,\mathbf{R}) - \vec{\xi}_{a_1}(Y,\mathbf{R})\right) \right\| \right\}.$$

The first four terms on the right hand side are bounded using (B.15) and the fact that the characteristic size of the solid particles is such that $h_{s,I} \geq \max(\|\bar{a}_2 - \bar{a}_1\|, \|\bar{a}_3 - \bar{a}_1\|)$. Developing the lest terms, we obtain three contributions which can be estimated separately. For instance, the first contribution is bounded as

$$\|\vec{\xi}_{a_1}(X,\mathbf{Q}) \wedge \vec{\xi}_{a_3}(X,\mathbf{Q}) - \vec{\xi}_{a_1}(Y,\mathbf{R}) \wedge \vec{\xi}_{a_3}(Y,\mathbf{R})\|$$
$$= \left\| \vec{\xi}_{a_1} \wedge (X,\mathbf{Q})\left(\vec{\xi}_{a_3}(X,\mathbf{Q}) - \vec{\xi}_{a_3}(Y,\mathbf{R})\right) + \vec{\xi}_{a_3} \wedge (Y,\mathbf{R})\left(\vec{\xi}_{a_1}(X,\mathbf{Q}) - \vec{\xi}_{a_1}(Y,\mathbf{R})\right) \right\|$$
$$\leq 2h_{s,I}\|(X-Y,\mathbf{Q}-\mathbf{R})\|_\infty,$$

where we have used (B.15) and the solid CFL condition on displacement which yields $\|\xi_{a_i}(X,\mathbf{Q})\| \leq h_{s,I}$, $\|\xi_{a_i}(Y,\mathbf{R})\| \leq h_{s,I}$ for all $i \in \{1,2,3\}$. Recollecting the above bounds, we infer that

$$\|\vec{F}_{\mathcal{F},\,\text{fluid}}(X,\mathbf{Q}) - \vec{F}_{\mathcal{F},\,\text{fluid}}(Y,\mathbf{R})\| \leq 5\bar{p}_\mathcal{F}^n h_{s,I}\|(X-Y,\mathbf{Q}-\mathbf{R})\|_\infty. \tag{B.16}$$

As a result, the positions of the center of mass verify

$$\|\chi_{p,I}(X,\mathbf{Q}) - \chi_{p,I}(Y,\mathbf{R})\| \leq \frac{5h_{s,I}\Delta t^2}{2m_I} \sum_{\mathcal{F}\in\mathfrak{F}_I} \bar{p}_\mathcal{F}^n \|(X-Y,\mathbf{Q}-\mathbf{R})\|_\infty.$$

Using (B.6) to bound m_I, we infer that

$$\|\chi_{p,I}(X,\mathbf{Q}) - \chi_{p,I}(Y,\mathbf{R})\| \leq \left\{ \frac{15}{8\pi} \frac{h_{s,I}}{\sigma_{s,I}} \frac{\Delta t^2}{\sigma_{s,I}^2} \sum_{\mathcal{F}\in\mathfrak{F}_I} \frac{\bar{p}_\mathcal{F}^n}{\rho_{s,I}} \right\} \|(X-Y,\mathbf{Q}-\mathbf{R})\|_\infty. \tag{B.17}$$

B.3. Estimate on the rotation

Using the bound (B.16) on the force, a lengthy but straightforward computation similar to the estimate of the fluid pressure force (see [26] for details) yields

$$\|\vec{\mathcal{M}}_{I,\,\text{fluid}}(X,\mathbf{Q}) - \vec{\mathcal{M}}_{I,\,\text{fluid}}(Y,\mathbf{R})\| \leq \sum_{\mathcal{F}\in\mathfrak{F}_I} 11\bar{p}_\mathcal{F}^n h_{s,I}^2 \|(X-Y,\mathbf{Q}-\mathbf{R})\|_\infty.$$

Owing to the construction of the Lagrange multiplier $\mathbf{\Upsilon}_I$, recalling the constant C from (27), we show in Section B.4 that

$$\|\mathbf{\Upsilon}_I(X,\mathbf{Q}) - \mathbf{\Upsilon}_I(Y,\mathbf{R})\| \leq C\|\vec{\mathcal{M}}_{I,\,\text{fluid}}(X,\mathbf{Q}) - \vec{\mathcal{M}}_{I,\,\text{fluid}}(Y,\mathbf{R})\|.$$

Observing that $\mathbf{j}: \mathbb{R}^3 \to \mathbb{R}^{3\times3}$ is a linear isometry, the rotation matrices verify

$$\|\chi_{r,I}(X,\mathbf{Q}) - \chi_{r,I}(Y,\mathbf{R})\| \leq \frac{11(1+2C)h_{s,I}^2\Delta t^2}{4}\|\mathbf{D}_I^{-1}\| \sum_{\mathcal{F}\in\mathfrak{F}_I} \bar{p}_\mathcal{F}^n\|(X-Y,\mathbf{Q}-\mathbf{R})\|_\infty.$$

Finally, using (B.6) to bound $\mathbf{D}_I$, the rotation matrices verify

$$\|\chi_{r,I}(X,\mathbf{Q}) - \chi_{r,I}(Y,\mathbf{R})\| \leq \left\{ \frac{165(1+2C)}{16\pi} \frac{h_{s,I}^3}{\rho_{s,I}\sigma_{s,I}^3} \frac{\Delta t^2}{\sigma_{s,I}^2} \sum_{\mathcal{F}\in\mathfrak{F}_I} \bar{p}_\mathcal{F}^n \right\} \|(X-Y,\mathbf{Q}-\mathbf{R})\|_\infty. \tag{B.18}$$

Collecting (B.17) and (B.18), we obtain

$$\|\chi(X,\mathbf{Q}) - \chi(Y,\mathbf{R})\|_\infty \leq \max_I \left\{ \left(\frac{15}{8\pi} \frac{h_{s,I}}{\sigma_{s,I}} + \frac{165(1+2C)}{16\pi} \frac{h_{s,I}^3}{\sigma_{s,I}^3} \right) \frac{\Delta t^2}{\sigma_{s,I}^2} \sum_{\mathcal{F}\in\mathfrak{F}_I} \frac{\bar{p}_\mathcal{F}^n}{\rho_{s,I}} \right\} \|(X-Y,\mathbf{Q}-\mathbf{R})\|_\infty.$$

As a result, the map χ is contracting with respect to the norm $\|\,\|_\infty$ under the CFL condition (28).

B.4. Estimate on the Lagrange multiplier in terms of torque

In the estimate on rotation, we have used the control of the Lagrange multiplier $\mathbf{\Upsilon}$ by the torque $\vec{\mathcal{M}}$. We prove this result herein. Owing to (B.14), we can rewrite the difference between two rotation matrices $\chi_{r,I}(X,\mathbf{Q})$ and $\chi_{r,I}(Y,\mathbf{R})$ as follows:

$$(\chi_{r,I}(X,\mathbf{Q}) - \chi_{r,I}(Y,\mathbf{R}))(\mathbf{Q}_I^n)^t \left(\mathbf{Q}_I^n \mathbf{D}_I (\mathbf{Q}_I^n)^t \right)$$
$$= \frac{\Delta t^2}{4} \left(\mathbf{j}(\vec{\mathcal{M}}_{I,\,\text{fluid}}(X,\mathbf{Q})) - \mathbf{j}(\vec{\mathcal{M}}_{I,\,\text{fluid}}(Y,\mathbf{R})) + 2\mathbf{\Upsilon}_I(X,\mathbf{Q}) - 2\mathbf{\Upsilon}_I(Y,\mathbf{R}) \right). \tag{B.19}$$

The left-hand side of (B.19) is composed of the product of differences between one time step incremental rotation matrices by the rotated matrix $\mathbf{D}_I$. Since $\mathbf{D}_I$ is real symmetric, up to changing matrix $\mathbf{Q}_I^n$ (which does not affect the estimate), it is possible to assume that $\mathbf{Q}_I^n \mathbf{D}_I (\mathbf{Q}_I^n)^t = \mathrm{diag}(d_1, d_2, d_3)$ (we omit the index I in d_i for simplicity). We write the incremental rotation matrices using the quaternion notation [29, Sec. VII.5],

$$\chi_{r,I}(X, \mathbf{Q})(\mathbf{Q}_I^n)^t = \mathbf{I} + 2e_0 \mathbf{j}(\vec{e}) + 2\mathbf{j}(\vec{e})^2, \quad e_0 = \sqrt{1 - \|\vec{e}\|^2},$$

$$\chi_{r,I}(Y, \mathbf{R})(\mathbf{Q}_I^n)^t = \mathbf{I} + 2f_0 \mathbf{j}(\vec{f}) + 2\mathbf{j}(\vec{f})^2, \quad f_0 = \sqrt{1 - \|\vec{f}\|^2},$$

where $\vec{e}$ and $\vec{f}$ represent a rotation vector: their direction indicates the axis of rotation and their magnitude is related to the angle of rotation θ by $\|e\| = \sin(\frac{\theta}{2})$.

Since $\mathbf{j}(\vec{M})$ is skew-symmetric and $\mathbf{\Upsilon}$ is symmetric, the right-hand side of (B.19) offers a decomposition of the left-hand side into its skew-symmetric and symmetric parts. Therefore, it can be checked that

$$\frac{\Delta t^2}{4}(\vec{\mathcal{M}}_{I,\,\text{fluid}}(X, \mathbf{Q}) - \vec{\mathcal{M}}_{I,\,\text{fluid}}(Y, \mathbf{R})) = \begin{pmatrix} (d_2 + d_3)(e_0 e_1 - f_0 f_1) + (d_2 - d_3)(e_2 e_3 - f_2 f_3) \\ (d_1 + d_3)(e_0 e_2 - f_0 f_2) + (d_3 - d_1)(e_1 e_3 - f_1 f_3) \\ (d_1 + d_2)(e_0 e_3 - f_0 f_3) + (d_1 - d_2)(e_1 e_2 - f_1 f_2) \end{pmatrix},$$

and that, for all $i, j \in \{1, 2, 3\}$,

$$\frac{\Delta t^2}{2}(\mathbf{\Upsilon}_I(X, \mathbf{Q}) - \mathbf{\Upsilon}_I(Y, \mathbf{R}))_{ij} = \begin{cases} -d_i(\|\vec{e}\|^2 - e_i^2 - \|\vec{f}\|^2 + f_i^2) & \text{if } i = j, \\ (d_i - d_j)(e_0 e_k - f_0 f_k) + (d_i + d_j)(e_i e_j - f_i f_j) & \text{if } (i, j, k) \\ \text{is an even permutation of } (1, 2, 3). \end{cases}$$

We introduce the Frobenius norm of a matrix $\|A\|_F^2 = \sum_{i,j=1}^3 A_{ij}^2$ and notice that $\|A\| \leq \|A\|_F$. Since the maximal angle of the incremental rotation for one time step is $\frac{\pi}{8}$ owing to the solid CFL condition and noticing that $\|\vec{e}\| \leq \sin(\frac{\theta}{2}) = \frac{1}{2}\sqrt{2 - \sqrt{2 + \sqrt{2}}}$, we set $\beta = \frac{1}{4}(2 - \sqrt{2 + \sqrt{2}})$ in Lemma (E.1) of [25] and obtain that $|e_0 - f_0| \leq \sqrt{\frac{\beta}{1-\beta}}\|\vec{e} - \vec{f}\|$ and $|e_0| \geq \sqrt{1 - \beta}$. Since $\frac{2\sqrt{\beta(1-\beta)}}{1-2\beta} = \sqrt{2} - 1 < 1$ and $d_i > 0$ for all $i \in \{1, 2, 3\}$, straightforward inequalities yield (see [26] for details)

$$\|\mathbf{\Upsilon}_I(X, \mathbf{Q}) - \mathbf{\Upsilon}_I(Y, \mathbf{R})\|_F^2 \leq \left(3 + \frac{1}{2}\frac{h_{s,I}^5}{\sigma_{s,I}^5}\right)\|\vec{\mathcal{M}}_{I,\,\text{fluid}}(X, \mathbf{Q}) - \vec{\mathcal{M}}_{I,\,\text{fluid}}(Y, \mathbf{R})\|^2.$$

References

[1] A. Soria, F. Casadei, Arbitrary Lagrangian–Eulerian multicomponent compressible flow with fluid–structure interaction, Int. J. Numer. Methods Fluids 25 (11) (1997) 1263–1284.

[2] K. Wang, A. Rallu, J.F. Gerbeau, C. Farhat, Algorithms for interface treatment and load computation in embedded boundary methods for fluid and fluid–structure interaction problems, Int. J. Numer. Methods Fluids 67 (9) (2011) 1175–1206.

[3] N. Favrie, S.L. Gavrilyuk, R. Saurel, Solid–fluid diffuse interface model in cases of extreme deformations, J. Comput. Phys. 228 (16) (2009) 6037–6077.

[4] G.H. Miller, P. Colella, A conservative three-dimensional Eulerian method for coupled solid–fluid shock capturing, J. Comput. Phys. 183 (1) (2002) 26–82.

[5] S.R. Idelsohn, J. Marti, A. Limache, E. Oñate, Unified Lagrangian formulation for elastic solids and incompressible fluids: application to fluid–structure interaction problems via the PFEM, Comput. Methods Appl. Mech. Eng. 197 (19) (2008) 1762–1776.

[6] P.B. Ryzhakov, R. Rossi, S.R. Idelsohn, E. Oñate, A monolithic Lagrangian approach for fluid–structure interaction problems, Comput. Mech. 46 (6) (2010) 883–899.

[7] J. Donea, S. Giuliani, J.P. Halleux, An arbitrary Lagrangian–Eulerian finite element method for transient dynamic fluid–structure interactions, Comput. Methods Appl. Mech. Eng. 33 (1) (1982) 689–723.

[8] P. Le Tallec, J. Mouro, Fluid structure interaction with large structural displacements, Comput. Methods Appl. Mech. Eng. 190 (24) (2001) 3039–3067.

[9] Z. Dragojlovic, F. Najmabadi, M. Day, An embedded boundary method for viscous, conducting compressible flow, J. Comput. Phys. 216 (1) (2006) 37–51.

[10] J. Falcovitz, G. Alfandary, G. Hanoch, A two-dimensional conservation laws scheme for compressible flows with moving boundaries, J. Comput. Phys. 138 (1) (1997) 83–102.

[11] R.B. Pember, J.B. Bell, P. Colella, W.Y. Crutchfield, M.L. Welcome, An adaptive Cartesian grid method for unsteady compressible flow in irregular regions, J. Comput. Phys. 120 (2) (1995) 278–304.

[12] C.S. Peskin, Numerical analysis of blood flow in the heart, J. Comput. Phys. 25 (3) (1977) 220–252.

[13] P. De Palma, M.D. De Tullio, G. Pascazio, M. Napolitano, An immersed-boundary method for compressible viscous flows, Comput. Fluids 35 (7) (2006) 693–702.

[14] P. Colella, D.T. Graves, B.J. Keen, D. Modiano, A Cartesian grid embedded boundary method for hyperbolic conservation laws, J. Comput. Phys. 211 (1) (2006) 347–366.

[15] X.Y. Hu, B.C. Khoo, N.A. Adams, F.L. Huang, A conservative interface method for compressible flows, J. Comput. Phys. 219 (2) (2006) 553–578.

[16] C. Farhat, A. Rallu, S. Shankaran, A higher-order generalized ghost fluid method for the poor for the three-dimensional two-phase flow computation of underwater implosions, J. Comput. Phys. 227 (16) (2008) 7674–7700.

[17] R.P. Fedkiw, Coupling an Eulerian fluid calculation to a Lagrangian solid calculation with the ghost fluid method, J. Comput. Phys. 175 (1) (2002) 200–224.

[18] R. Abgrall, S. Karni, Ghost-fluids for the poor: a single fluid algorithm for multifluids, in: Hyperbolic Problems: Theory, Numerics, Applications, vols. I, II, Magdeburg, 2000, in: Int. Ser. Numer. Math., vol. 141, Birkhäuser, 2001, pp. 1–10.

[19] W.F. Noh, Fundamental methods of hydrodynamics, Methods Comput. Phys. 3 (1964) 117–179.

[20] J. Grétarsson, R. Fedkiw, Fully conservative, robust treatment of thin shell fluid–structure interactions in compressible flows, J. Comput. Phys. 245 (2013) 160–204.

[21] L. Monasse, V. Daru, C. Mariotti, S. Piperno, C. Tenaud, A conservative coupling algorithm between a compressible flow and a rigid body using an embedded boundary method, J. Comput. Phys. 231 (7) (2012) 2977–2994.

[22] M.A. Puscas, L. Monasse, A three-dimensional conservative coupling method between an inviscid compressible flow and a moving rigid solid, submitted for publication, http://hal.archives-ouvertes.fr/hal-00974602.

[23] V. Daru, C. Tenaud, High order one-step monotonicity-preserving schemes for unsteady compressible flow calculations, J. Comput. Phys. 193 (2) (2004) 563–594.

[24] C. Mariotti, L. Monasse, From General Mechanics to Discontinuity, Unified Approach to Elasticity, Presses des Ponts, 2012.

[25] L. Monasse, C. Mariotti, An energy-preserving discrete element method for elastodynamics, ESAIM: Math. Model. Numer. Anal. 46 (2012) 1527–1553.

[26] M.A. Puscas, Development of a numerical coupling method between an inviscid compressible fluid and a deformable structure with possible fragmentation, PhD thesis, University Paris-Est, France, 2014.

[27] J.T. Grétarsson, N. Kwatra, R. Fedkiw, Numerically stable fluid–structure interactions between compressible flow and solid structures, J. Comput. Phys. 230 (8) (2011) 3062–3084.

[28] T.J. Poinsot, S.K. Lele, Boundary conditions for direct simulations of compressible viscous flows, J. Comput. Phys. 101 (1992) 104–129.

[29] E. Hairer, C. Lubich, G. Wanner, Geometric Numerical Integration: Structure-Preserving Algorithms for Ordinary Differential Equations, 2nd edition, Springer Ser. Comput. Math., vol. 31, Springer-Verlag, 2006.